

Chronic Loss of CA2 Transmission Leads to Hippocampal Hyperexcitability

Highlights

- CA2 silencing results in increased excitability of the recurrent CA3 network
- A loss of CA2 transmission leads to unexpected network pathophysiology
- Spatially triggered network hyperexcitability events mimic single place fields
- CA2 driven feedforward inhibition in CA3 is crucial for hippocampal E/I balance

Authors

Roman Boehringer, Denis Polygalov, Arthur J.Y. Huang, ..., Rebecca A. Piskorowski, Vivien Chevalleyre, Thomas J. McHugh

Correspondence

tjmchugh@brain.riken.jp

In Brief

Boehringer et al. show that silencing CA2 pyramidal cells leads to hyperexcitability in CA3 and a novel pathophysiology manifesting as spatially triggered hippocampal network population discharges. This establishes a key role of CA2-recruited inhibition in CA3 in maintaining hippocampal E/I balance.



Chronic Loss of CA2 Transmission Leads to Hippocampal Hyperexcitability

Roman Boehringer,¹ Denis Polygalov,¹ Arthur J.Y. Huang,¹ Steven J. Middleton,¹ Vincent Robert,² Marie E. Wintzer,¹ Rebecca A. Piskorowski,² Vivien Chevalyere,² and Thomas J. McHugh^{1,3,4,*}

¹Laboratory for Circuit and Behavioral Physiology, RIKEN Brain Science Institute, 2-1 Hirosawa, Wakoshi, Saitama 351-0198, Japan

²Team of Synaptic Plasticity and Neural Networks, Center of Psychiatry and Neuroscience, Inserm U894, Université Paris Descartes, Sorbonne Paris Cité, 75014 Paris, France

³Department of Life Sciences, Graduate School of Arts and Sciences, University of Tokyo, Tokyo 153-8902, Japan

⁴Lead Contact

*Correspondence: tjmchugh@brain.riken.jp

<http://dx.doi.org/10.1016/j.neuron.2017.04.014>

SUMMARY

Hippocampal CA2 pyramidal cells project into both the neighboring CA1 and CA3 subfields, leaving them well positioned to influence network physiology and information processing for memory and space. While recent work has suggested unique roles for CA2, including encoding position during immobility and generating ripple oscillations, an interventional examination of the integrative functions of these connections has yet to be reported. Here we demonstrate that CA2 recruits feedforward inhibition in CA3 and that chronic genetically engineered shutdown of CA2-pyramidal-cell synaptic transmission consequently results in increased excitability of the recurrent CA3 network. In behaving mice, this led to spatially triggered episodes of network-wide hyperexcitability during exploration accompanied by the emergence of high-frequency discharges during rest. These findings reveal CA2 as a regulator of network processing in hippocampus and suggest that CA2-mediated inhibition in CA3 plays a key role in establishing the dynamic excitatory and inhibitory balance required for proper network function.

INTRODUCTION

The hippocampus plays a key role in spatial, temporal, and episodic memory, achieving its integrative function via a careful balance of excitation and inhibition (E/I) and precise timing of its inputs and outputs (Ahmed and Mehta, 2009; Royer et al., 2012; Squire et al., 2004). Classically, the flow of information through the structure has been described as progressing from the entorhinal cortex (EC) to the dentate gyrus (DG), then sequentially along the CA3/CA2/CA1 axis; however, anatomy and physiology suggest a more complex regulation of multiple circuits that can interact to drive plasticity and memory (Moser et al., 2008; Sekino et al., 1997). Interest in the CA2 subregion has recently intensified, since accumulating evidence has led to proposals

of its multiple novel roles in hippocampal function (Dudek et al., 2016; Jones and McHugh, 2011). These data suggest that CA2 is involved in novelty detection (Alexander et al., 2016; Wintzer et al., 2014), social memory (Hitti and Siegelbaum, 2014), and ripple generation (Oliva et al., 2016a), and that it contributes to spatial coding in a manner distinct from CA1 and CA3 (Kay et al., 2016; Lee et al., 2015; Lu et al., 2015; Mankin et al., 2015; Oliva et al., 2016b). Anatomically, CA2 pyramidal cells (PCs) receive excitatory input from layer 2 of the EC (EC2), CA3 PCs, and DG granule cells, as well as from other CA2 PCs (Cui et al., 2013; Kohara et al., 2014). In contrast to CA1, input from CA3 to CA2 PCs is weak, often resulting in net inhibition (Chevalyere and Siegelbaum, 2010; Valero et al., 2015), whereas even modest input from EC2 can robustly and rapidly activate CA2 PCs, leading to output that is temporally coincident with the DG (Bartasaghi and Gessi, 2004; Sun et al., 2014). The axons of CA2 PCs have diverse synaptic targets within the hippocampal formation, synapsing both onto CA1 and CA3 neurons as well as projecting to the EC and subcortical structures involved in the generation of the theta oscillation: the supramammillary nucleus and the medial septum (Cui et al., 2013; Kohara et al., 2014; Rowland et al., 2013). This anatomy and physiology points to CA2 as an integrator or modulator of information flow within the circuit; however, the physiological consequences of impairing CA2 function remain unknown.

Here we address the role of CA2 in hippocampal function by employing viral-mediated, CA2-PC-restricted silencing of synaptic transmission both chronically, via the expression of the tetanus neurotoxin (TeTX) light chain, and acutely, via the activation of the G_i-coupled DREADD (hM₄D) receptors. Using a combination of in vitro physiology and in vivo recording in behaving mice, we reveal a novel role for CA2 excitatory transmission in triggering robust feedforward inhibition (FFI) in CA3 that works to dampen excitation and promote sparsity in the hippocampal network. While acute DREADD-mediated inhibition of CA2 transmission did not lead to large changes in circuit excitability, it did result in an increase in the spatial concentration of CA1 and CA3 PC spiking. More dramatically, chronic blockade of CA2 transmission led to hyperexcitability in the recurrent CA3 network, resulting in distinct pathophysiological states both during exploration and rest. Our data suggest a key role of CA2 in establishing the dynamic E/I balance required for proper network function.

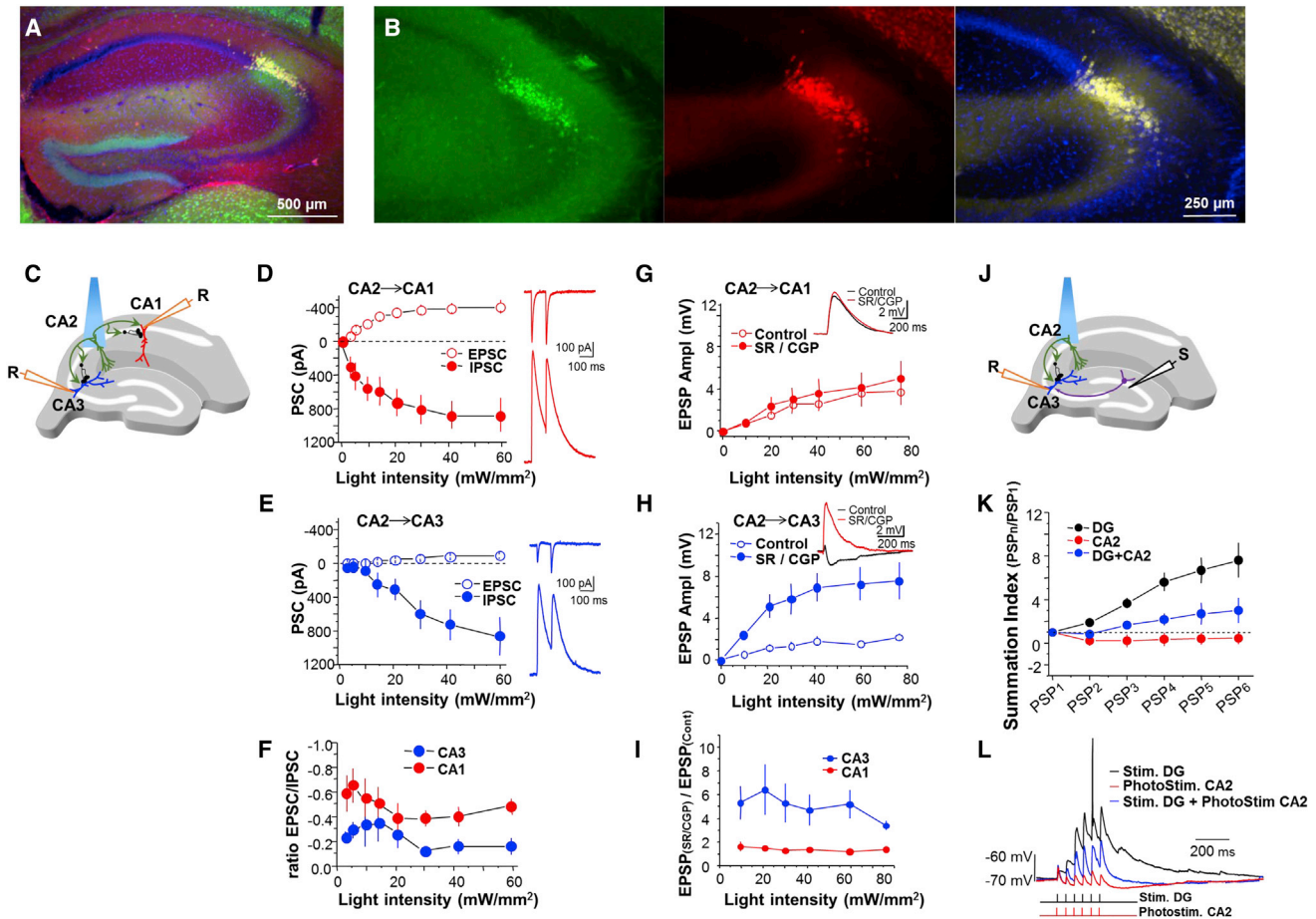


Figure 1. CA2 Output Recruits Inhibition in CA3 and Filters Network Excitability

- (A) Double immunohistochemical labeling reveals robust Cre recombinase expression in CA2 pyramidal cells (PCs) of the *Cacng5-Cre* mouse. Green, α -Cre; red, α -PCP4, a CA2-PC marker; blue, DAPI.
- (B) 10 \times image of dorsal CA2 of a *Cacng5-Cre* mouse. Left, α -Cre; center, α -PCP4; right, overlay.
- (C) Diagram of the acute hippocampal slice whole-cell recording configuration. ChR2 was selectively expressed in CA2 PCs (green), permitting selective light-evoked stimulation. Whole-cell voltage clamp recordings were performed in CA1 (red) and CA3 (blue) PCs with Cs⁺ in the pipette solution, allowing for the measure of excitatory post-synaptic currents (EPSCs) at -70 mV and inhibitory post-synaptic currents (IPSCs) at $+10$ mV.
- (D) The light-evoked synaptic input from CA2 PCs onto CA1 PCs with either the EPSC (red open circles) or the IPSC (red filled circles) plotted as a function of light intensity. Right, example traces (top: EPSC, bottom: IPSC) at 30 mW.
- (E) The light-evoked synaptic input from CA2 PCs onto CA3 PCs with either the EPSC (blue open circles) or the IPSC (blue filled circles), plotted as a function of light intensity. Right, example traces at 30 mW.
- (F) Plot of the EPSC:IPSC ratio as a function of light intensity for CA1 PCs (red filled circles) and CA3 PCs (blue filled circles) reveals that CA2 PCs drive strong feedforward inhibition (FFI) to CA3 PCs as compared to CA1 PCs.
- (G) Whole-cell current-clamp recordings performed in CA1 PCs with intracellular K⁺ in the pipette reveal that CA2-CA1 excitation is unchanged by blockade of synaptic inhibition. The light-evoked EPSP amplitudes recorded in CA1 PCs are plotted as a function of 470 nm light with inhibitory transmission intact (open red circles) or blocked with 1 μ M SR95531 (GABA_A R antagonist) and 2 μ M CGP (GABA_B R antagonist filled; red circles). Example traces for both conditions at 30W are inset.
- (H) Whole-cell current clamp recordings performed in CA3 PCs reveal a strong FFI controls excitation driven by light stimulation of CA2 inputs. Light-evoked EPSP amplitudes recorded in CA3 PCs are plotted as a function of 470 nm light with inhibitory transmission intact (open blue circles) or blocked with 1 μ M SR95531 and 2 μ M CGP (filled blue circles). Example traces for both conditions at 30 W are inset.
- (I) The ratio of EPSP amplitudes from light-evoked CA2 inputs with inhibition blocked (SR/CGP) and inhibition intact for CA1 PCs (red circles) and CA3 PCs (blue circles), plotted as a function of light intensity. The increase in the ratio in CA3 PCs indicates that FFI from CA2 is sufficient to directly modulate CA3 output.
- (J) Diagram of the recording configuration in hippocampal slices with ChR2 selectively expressed in CA2 PCs. Whole-cell current-clamp recordings were performed in CA3 PCs. Pulses of 470 nm light were used to evoke a series of PSPs from CA2 inputs, and a focal electrical stimulation pipette evoked PSPs from the DG inputs, both alone and together.
- (K) Plot of the summation index (PSP_n/PSP₁) as a function of stimulus number for DG inputs alone (black circles), CA2 inputs (red circles), and DG and CA2 inputs together (blue circles).
- (L) Representative traces of PSPs evoked by focal electrical stimulation (Stim. DG) and light stimulation (PhotoStim. CA2) of CA2 inputs, both alone and together (Stim. DG + PhotoStim. CA2).

(legend continued on next page)

RESULTS

CA2 Gates Hippocampal Excitability via Feedforward Inhibition

While previous work has suggested that CA2 PCs target excitatory neurons in CA1 and a mixed population of excitatory and inhibitory neurons in CA3 (Kohara et al., 2014), little is known about how CA2 may influence activity in these regions. To better characterize these local connections, we generated a transgenic line (*Cacng5-Cre*) in which Cre recombinase expression was restricted to CA2 PCs of the adult hippocampus, with lower expression levels observed in DG granule cells and scattered cells in CA1 (CA2-Cre; Figures 1A and 1B). Stereotaxic injection of a Cre-dependent, adeno-associated virus (AAV) expressing channelrhodopsin-2-EYFP (ChR2) into dorsal CA2 yielded highly specific expression in CA2 PCs and allowed us to employ optical stimulation *in vitro* to examine the local circuit effects resulting from CA2 activation (Figures 1C and S1). We first compared same-cell excitatory post-synaptic currents (EPSCs) and inhibitory post-synaptic currents (IPSCs) recorded from CA1 or CA3 PCs *in vitro* following ChR2-mediated excitation of CA2 PCs. Surprisingly, we found that CA2-PC inputs induced not only large excitatory currents, but also large inhibitory currents in CA1 (Figure 1D, $N = 4$, $n = 10$). In CA3, the pattern of evoked inhibition was similar to that of CA1; however, the excitatory currents were comparatively smaller at all stimulation intensities (Figure 1E, $N = 3$, $n = 5$). As a consequence, the E/I ratio was heavily skewed toward inhibition in CA3 (~7- to 10-fold) compared with CA1 (~2- to 3-fold, two-way repeated-measure ANOVA: $F_{1,17} = 5,728$, $p = 0.0028$ between CA1 and CA3; Figure 1F). To address whether CA2-mediated FFI was sufficient to dampen the excitatory drive from CA2, we monitored light-evoked excitatory post-synaptic potentials (EPSPs) in CA1 and CA3 before and after blocking inhibitory transmission. We found that the magnitude of light-evoked EPSPs in CA1 was not altered following blockade of both GABA_A and GABA_B receptors ($N = 4$, $n = 7$, two-way repeated-measure ANOVA: $F_{1,2} = 2.33$, $p = 0.26$), indicating that the FFI driven by CA2 PCs targets other synaptic inputs more distant from the soma (Figure 1G). In contrast, CA3 EPSPs were very small and truncated by large inhibitory post-synaptic potentials (IPSPs) in control conditions, and the application of GABA-receptor blockers resulted in a significant increase in EPSP amplitude ($N = 3$, $n = 5$, two-way repeated-measure ANOVA: $F_{1,3} = 17.6$, $p = 0.024$; Figure 1H). This increase of CA3 EPSPs (two-way repeated-measure ANOVA: $F_{1,4} = 12.9$, $p = 0.023$ CA3 x CA1) indicates that FFI from CA2 is sufficient to directly modulate CA3 output (Figure 1I).

To further explore the functional role of this FFI, we performed whole-cell current clamp recordings from CA3 PCs during electrical stimulation of the DG mossy fiber input, either alone or paired with optical stimulation of CA2. We found that trains of DG stimulation would readily summate, frequently resulting in

action potential firing; however, co-stimulation of CA2-PC inputs dramatically reduced summation ($N = 4$, $n = 8$, two-way repeated-measure ANOVA: $F_{1,6} = 23.9$, $p = 0.0017$; Figures 1J–1L). Together, these data demonstrate that CA2 PCs recruit FFI that can gate CA3 circuit excitability and suggest that silencing CA2 PCs would alter information transfer throughout the hippocampus.

Chronic Silencing of CA2 Transmission Results in an Increase in CA3 Recurrent Pathway Excitability

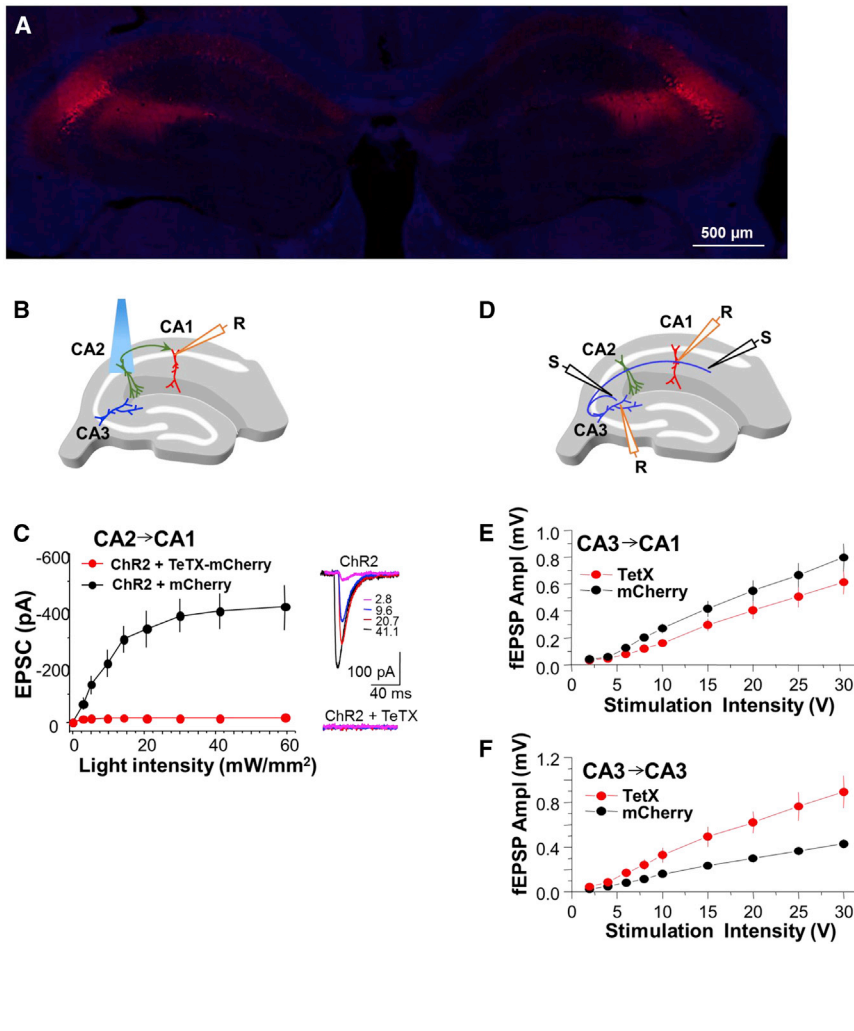
To examine how the loss of CA2 transmission impacts hippocampal physiology, we virally expressed the tetanus toxin light chain (TeTX) specifically in CA2 PCs to block synaptic transmission (Figure 2A). The efficacy of transmission blockade was first verified by injecting CA2-Cre mice with two viruses that expressed channelrhodopsin-2 (ChR2)-eYFP and TeTX-mCherry or, as a control, ChR2-eYFP and mCherry. Dorsal hippocampal slices were prepared 8–15 days post-injection, and CA1 PCs were recorded in whole-cell voltage clamp configuration to examine EPSCs originating from CA2-PC input. In control slices, light stimulation of ChR2-expressing CA2 PCs elicited robust EPSCs in CA1 PCs (Figure 2B, $N = 5$, $n = 13$). In contrast, no light-evoked synaptic transmission was detected when TeTX-mCherry was co-expressed even at maximal light intensity, demonstrating the high efficacy of TeTX in silencing synaptic transmission (Figure 2B, $N = 3$, $n = 16$, two-way repeated-measure ANOVA: $F_{1,4} = 31.08$, $p = 0.005$ compared to ChR2-alone condition).

Next, to assess the impact of chronic CA2 silencing on CA3 recurrent transmission and CA3 to CA1 transmission, we compared the input and output (I/O) curves in these circuits in hippocampal slices prepared from control mice expressing CA2-TeTX or mCherry (Figure 2D). While we observed a small but significant difference in CA3 to CA1 transmission between the groups (two-way repeated-measure ANOVA: $F_{1,19} = 4.52$, $p = 0.046$ between TeTX and mCherry; Figure 2E), we found a significant and large upward shift in the I/O curve in the CA3 recurrent network in slices from CA2-TeTX mice (two-way repeated-measure ANOVA: $F_{1,15} = 8.8$, $p = 0.0096$ between TeTX and mCherry; Figure 2F). These data suggest that a chronic loss of CA2 activity results in a hyperexcitability in the recurrent CA3 circuit.

CA2-TeTX Mice Exhibit Place-Triggered Network Hyperexcitability

To assess how the changes in the E/I balance in CA3 following chronic CA2 silencing affect *in vivo* hippocampal physiology, we injected CA2-Cre mice bilaterally with AAV expressing either TeTX-mCherry (CA2-TeTX; $N = 8$) or mCherry alone (control; $N = 9$) and fitted them with multi-tetrode recording drives targeting the hippocampus (Figures S1 and S2). Recordings began 1 week post-injection and were performed both during sleep

(L) Stimulation of DG (black trace) results in large summation of the PSP inputs into CA3 and AP firing, whereas stimulation of CA2 (red trace) results in no summation. Simultaneous stimulation of CA2 and DG inputs (blue trace) reduces the net depolarization and prevents AP firing, indicating that FFI recruited by CA2 is acting to prevent CA3 excitability. Black tick marks below show the timing of the DG stimulation, and red marks show the timing of the CA2 stimulation. All plots show mean \pm SEM. See also Figure S1 for additional viral expression data.



and quiet wakefulness in a small box and during exploration of linear tracks and open fields. CA2-TeTX mice displayed large, though transient, increases in broadband LFP power during exploration (Figure 3A). The onset of this phenotype varied from mouse to mouse (range: 6–12 days post-injection, 9.4 ± 0.7 days, mean \pm SEM) due to the inherent variability in the timing of virally expressed TeTX; thus, we defined the first day with observable increases in LFP power as the day of onset and aligned recording sessions to this day. The transient increases in power constituted $25.4 \pm 2.5\%$ of the total movement time and were associated with significant increases in total power (2–400 Hz), as well as power in the theta band (4–12 Hz), gamma band (30–90 Hz), and a high-frequency band (200–300 Hz) virtually absent in control conditions. Outside of these periods we found no difference in the LFP power spectrum compared to control mice (Figures 3A).

As LFP power—particularly in the theta band—can be modulated by animal velocity (Czurkó et al., 1999), we compared the speed of movement between groups. CA2-TeTX mice displayed a higher average velocity than did controls (control: 5.02 ± 0.26 cm/s; CA2-TeTX: 6.86 ± 0.55 cm/s; t test, $p = 0.002$); how-

ever, the correlation strength of velocity and theta power was unchanged (control: $r = 0.36 \pm 0.16$; CA2-TeTX: $r = 0.45 \pm 0.08$, Wilcoxon rank sum test, $p = 0.58$). Further, thresholding theta magnitude (3 SD above mean) within sessions revealed that LFP power increases were not correlated with specific velocities or accelerations (Figures S3A–S3C), but rather modulated as a function of position in both linear tracks and open fields (Figures 3B–3D, S3D, S3E, and S4). The coefficient of variation of theta power across space was significantly different between groups (control: 0.13 ± 0.03 , CA2-TeTX: 0.38 ± 0.05 , Mann-Whitney, $p < 0.00001$), indicating that increases in theta power were spatially restricted in CA2-TeTX mice. In CA1, these events were accompanied by high-frequency oscillations (HFO: 278.49 ± 1.63 Hz; $N = 4$, $n = 418$) tightly locked to the rising phase of theta (mean phase: $337.94 \pm 4.01^\circ$; Figures 3E and 3F). However, despite their similarity to spike-wave-type discharges often accompanying seizure activity (Pearce et al., 2014), this pathophysiology did not result in any observable acute behavioral changes (Movie S1). Although clearly encompassing a large portion of the hippocampal network (being detectable across all recording sites in the dorsal hippocampus), these location-specific hyperexcitability episodes frequently

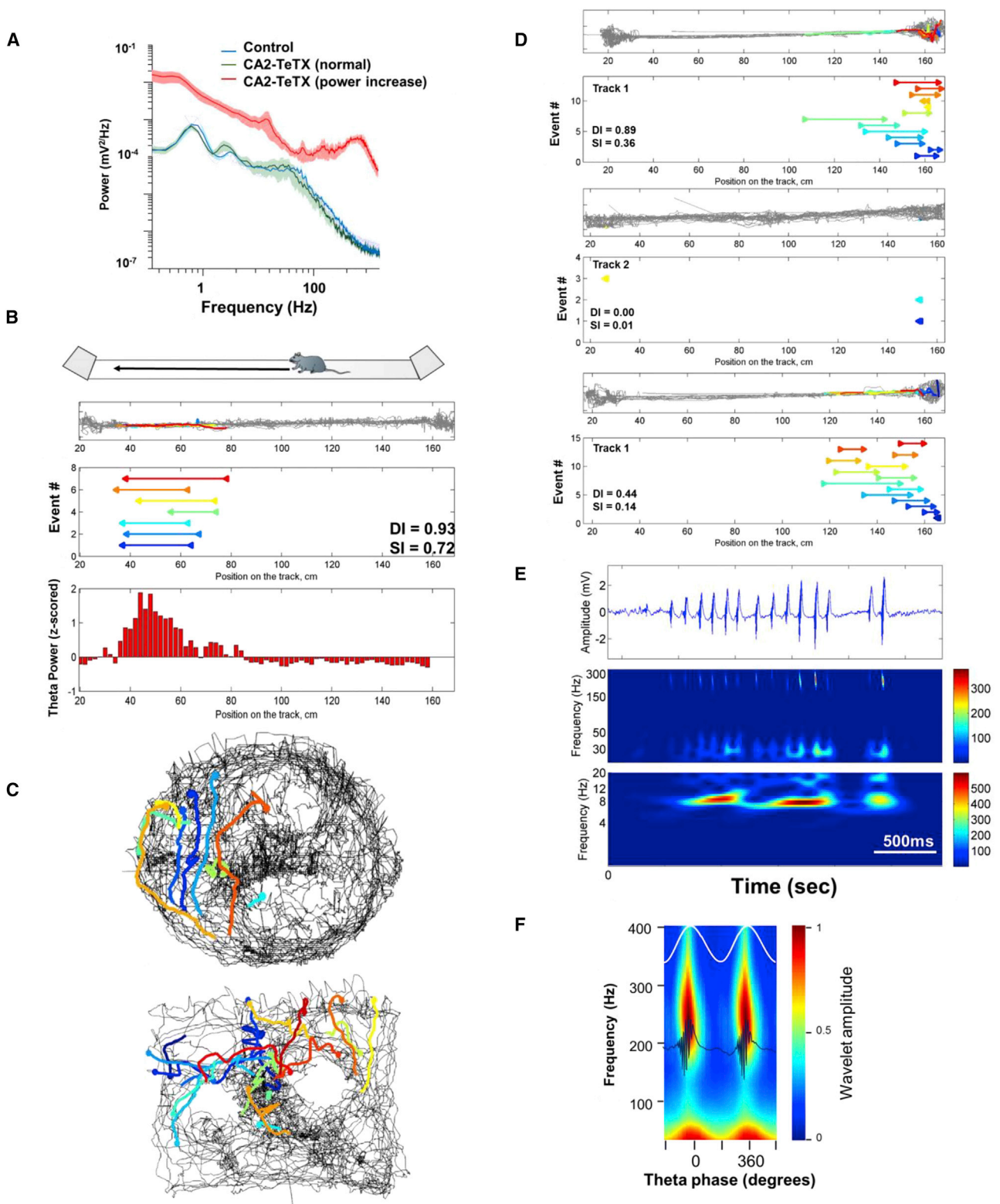


Figure 3. Silencing CA2 PCs Leads to Transient Increases in LFP Power with Properties Similar to Place Fields

(A) Power-spectrum density curves of CA1 LFP recorded during exploration of the linear track for control mice (blue, N = 8) and CA2-TeTX mice (N = 5). The LFP from the CA2-TeTX mice was segregated into normal (green) and pathophysiological (red) periods and plotted separately. Plots show mean \pm SEM (shaded regions).

(legend continued on next page)

exhibited properties normally observed in single-place cells. On average, their duration was 1.82 ± 0.10 s ($N = 8$ mice, $n = 32$ sessions), equating to approximately 15%–20% of the track; by comparison, average CA1 place-field size in control mice was $20.6\% \pm 0.8\%$ (Table S1). Further, they were repeatedly triggered by specific locations in a single context across multiple sessions within a day, exhibited directionality on a linear track, remapped between similar but distinct contexts, and/or were absent in some contexts (Figures 3B–3D and S4). Typically, hippocampal LFP recorded at a single site does not carry any discernible spatial information (Agarwal et al., 2014); however, in CA2-TeTX mice, CA1 theta power carried significant directional information (directionality index: control 0.03 ± 0.004 , CA2-TeTX 0.19 ± 0.02 , Mann-Whitney, $p < 0.0001$) and spatial information (spatial information: control 0.02 ± 0.002 bits per s, CA2-TeTX 0.39 ± 0.056 bits per s, Mann-Whitney, $p < 0.0001$).

Despite the profound network phenotype seen in the LFP and the changes in CA3 circuit excitability *in vitro*, the alterations we observed on the level of single PCs in CA1 and CA3 were comparatively subtle. While chronic CA2 silencing resulted in decreases in the spatial information of place cells in all CA regions (Figure 4A, Table S1), there were no significant changes in the average firing rates of CA1 and CA3 PCs across the entire session. However, when we examined the time periods directly preceding the onset of spatially triggered network hyperexcitability, we observed a clear ramping increase of PC activity (Figure 4B). This could be seen both as an increase in the firing rate across all PCs as well as an increase in the fraction of neurons active during that period. This transient, spatially triggered excitability across the ensemble suggests that both in-field and out-of-field spiking contributed to the onset of the suprathreshold population events detected in the LFP. Additionally, we addressed the possibility that the change in E/I balance resulting from CA2 silencing would impact not just excitability, but also the precise timing of neuronal activity. We examined the spike timing of significantly theta-modulated CA3 PCs referenced to the CA1 theta oscillation, focusing on neurons recorded in CA3a, although the effects were similar in CA3c (Figure S5). Following CA2-PC silencing, there was no change in the fraction of CA3a PCs demonstrating significant theta modulation (control: 57/71, 80.3%; CA2-TeTX:

31/47, 66.0%, Chi-square test, $p = 0.08$) or in their strength of modulation (mean resultant length vector [MRL]: control: 0.29 ± 0.01 , CA2-TeTX: 0.33 ± 0.03 , Mann-Whitney $p = 0.65$). However, across the population of neurons in the CA2-TeTX mice, there was a shift in the spike-firing preference to later theta phases (Kuiper Test, $p = 0.005$; Figure 4C). In control mice, 77.2% (44/57) of CA3 PCs preferred phases prior to the peak of CA1 theta; however, in the CA2-TeTX mice, this was significantly reduced to 54.8% (17/31; Chi-square test, $p = 0.03$). This shift persisted when we calculated spike-firing probability across phase for all CA3a-PC spikes, regardless of modulation-index significance, with the maximum probability in the CA2-TeTX mice occurring just after the theta peak (control $279.8 \pm 2.0^\circ$; CA2-TeTX post $41.0 \pm 1.3^\circ$), which is typically a period of enhanced inhibition.

Acute Inhibition of CA2 Pyramidal Cells Impacts the Spatial Distribution of Ensemble Spiking

Given the alterations in physiology we observed following chronic CA2 blockade, we next sought to determine which, if any, of the phenotypes could be replicated with acute CA2 inhibition. To this end, we injected CA2-Cre mice bilaterally with AAV expressing either the inhibitory G_i-coupled DREADD receptor and mCherry (hM4Di-mCherry; Armbruster et al., 2007; CA2-DREADD; $N = 7$) or mCherry alone (control; $N = 6$) and fitted them with multi-tetrode recording drives targeting all three CA fields of the hippocampus (Figure 5A). At 2 weeks following surgery, we recorded single-unit activity and LFP while the mice explored a familiar linear track both before and after systemic injection of the synthetic DREADD ligand clozapine-N-oxide (CNO; 2 mg/kg). Comparing baseline mean firing rates of PCs before and after CNO injection confirmed a specific and significant inhibition of CA2-PC spiking (normalized change in mean rate, CA2-DREADD: -0.76 ± 0.02 ; control: -0.14 ± 0.04 ; $p < 0.0001$; Figure 5B). Despite this inhibition, we did not observe the spatially triggered network hyperexcitability events present in the CA2-TeTX mice, nor did we see significant changes in CA1- or CA3-PC excitability on the single-cell level (Table S2).

One advantage of the DREADD system is that the acute nature of the manipulation allowed us to compare the activity of the

(B) Upper: during linear track exploration, spatially triggered network hyperexcitability events were detected by increases in theta magnitude (3 SD > mean) and color-coded by order of occurrence within each session from blue (first) to red (last). Each arrow represents a single event and indicates the direction of the mouse and the spatial location of the increase in theta magnitude. Lower right corner: values for the directionality index (DI) and spatial information (SI; bits per s) calculated from theta power and magnitude, respectively. Lower: average normalized theta power, independent of direction, plotted across position for the same session demonstrates the spatial nature of the increases.

(C) Examples of location-specific theta magnitude increase in an open-field environment. These two sessions were recorded in the same mouse on the same day. Black lines represent the path of the mouse and colored lines indicate location of increases, coded by order of occurrence within the session from blue (first) to red (last).

(D) Location-specific theta magnitude increases show stability and context specificity. Three run sessions recorded in the same mouse across 90 min. The first and third sessions of the day (top and bottom) were recorded on the same track. Note the stability in the location of the increases in theta magnitude. The second session (middle) was recorded on a distinct track, where no clear theta magnitude increases were observed.

(E) Example of a single spatially triggered network hyperexcitability event. At top, raw LFP is shown. In center, wavelet transform of the event in the 20–300 Hz band reveals a short-duration high frequency component accompanying the large increase in theta power visible in the lower panel (lower, wavelet transform in the 2–20 Hz band).

(F) The increase in power in the high-frequency component of the LFP band was tightly locked to the rising phase of the concurrent theta oscillation ($N = 5$). White trace (top) represents theta phase, and dark blue trace (center) is an example of the raw LFP. The increase in power in the high-frequency LFP band is represented by the increase in the z-scored wavelet amplitude, with red representing the peak value.

See also Figures S2, S3, and S4.

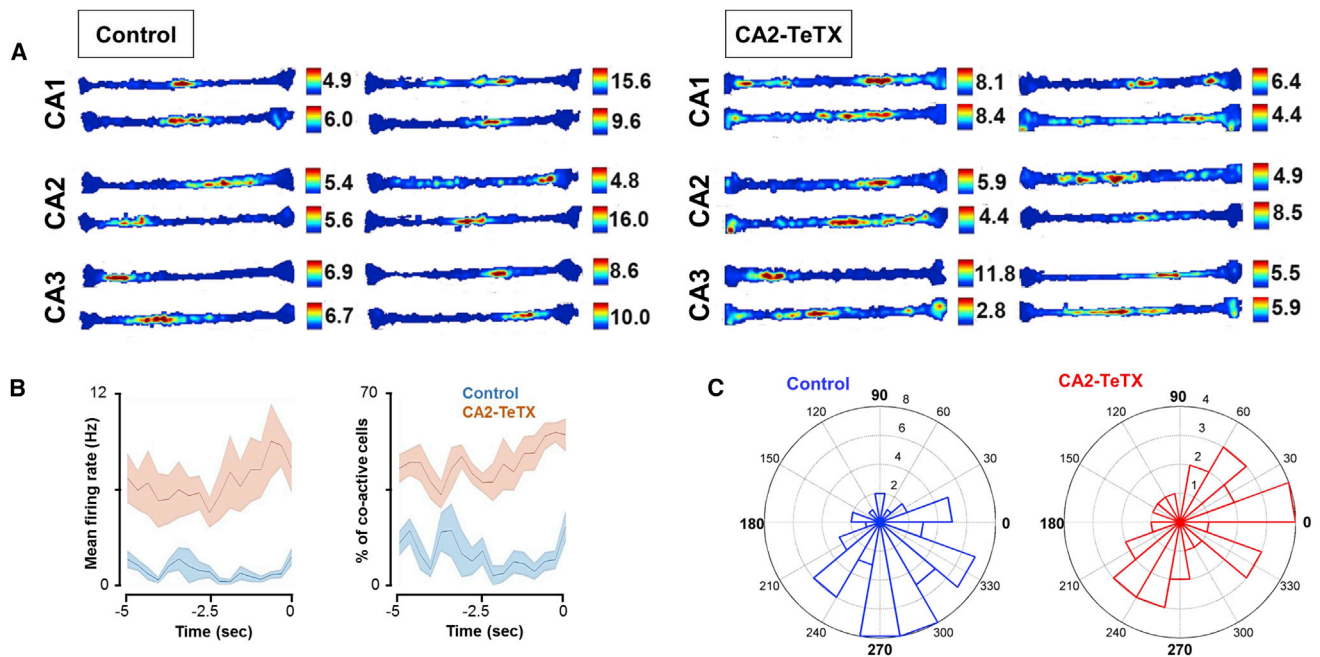


Figure 4. Changes in PC Spiking Following Chronic CA2 Silencing

(A) Example firing-rate maps of place cells from each CA region recorded in control (left) and CA2-TeTX (right) mice on a familiar linear track. The firing rate of each cell is plotted by position on the track. Each cell is scaled individually (value to the right indicates peak rate in Hz) with blue representing zero and red representing the peak rate. Although we did not observe a significant change in the mean firing rate and spatial coding was seen in both groups, the spatial specificity of CA1 and CA3 PCs was significantly poorer in the CA2-TeTX mice.

(B) CA1 and CA3 PC activity transiently increases prior to the onset of spatially triggered network hyperexcitability events. We examined the ensemble activity across all active PCs (CA1 and CA3) in the 5 s prior to the increase in theta magnitude in CA2-TeTX mice (red line) and in behaviorally equivalent periods in control mice (blue line). A clear ramping increase in the mean ensemble firing rate (left) and an increase in the fraction of active cells (neurons firing at least one spike in given temporal bin; right) could be seen in the CA2-TeTX mice prior to the onset of the population event. Plots show mean \pm SEM (shaded regions).

(C) A loss of CA2 transmission alters CA3 spike timing. The preferred firing phase of CA1 theta was calculated for all significantly theta-modulated CA3a PCs during exploration of the linear track. A circular histogram of these preferred phases demonstrates that the population of neurons in the CA2-TeTX mice shift their preference to later theta phases (blue, control; red, CA2-TeTX; 0/360, theta peak; 180, theta trough).

See [Table S1](#) for properties of CA PCs recorded in control and CA2-TeTX mice and [Figure S5](#) for analysis of the change in spike timing of CA3c PCs.

same population of neurons before and after CA2 inhibition. Given the spatially tuned and transient nature of the increases in circuit excitability we observed in CA2-TeTX PC spiking ([Figure 4B](#)), we asked whether we could find a similar effect following the partial DREADD-mediated shutdown by comparing the activity across the CA1 and CA3 ensemble before and after CNO injection. First we compared the correlation of the spatial firing of CA1 and CA3 place cells between the pre- and post-CNO sessions and found no difference between the CA2-DREADD and control mice (Pearson's r ; control CA1: 0.54 ± 0.02 , CA2-DREADD CA1: 0.55 ± 0.02 , $p = 0.88$; control CA3: 0.62 ± 0.05 , CA2-DREADD CA3: 0.65 ± 0.03 , $p = 0.65$). However, while CA2 inhibition did not alter the degree of spatial change between sessions, it did introduce an unexpected structure to these changes. Specifically, in the CA2-DREADD mice in the post-CNO session on the track, we observed the development of "hotspots" of multi-unit activity resulting from an increase in the concentration of CA1 and CA3 PC spiking ([Figure 5C](#)) and reminiscent of the spatially restricted PC ramping PC activity we observed in the CA2-TeTX mice. In contrast, no change in the spatial distribution of peak-ensemble activity was observed in control mice ([Figure 5D](#)). To investigate this further, we next

considered the subset of PCs that showed a significant shift in their peak firing location (>10 cm) between the pre- and post-CNO sessions. In the CA2-DREADD mice, we found a significant correlation between the proximity of a neuron's place field to the peak-ensemble firing location in the post-CNO session and the direction and magnitude of its firing rate change, while in the controls there was no such relationship ([Figure 5E](#); CA2-DREADD: $N = 7$, $n = 158$, $r = -0.58$, $p < 0.0001$; control: $N = 6$, $n = 149$, $r = -0.04$, $p = 0.75$; Fisher r -to- z comparison between groups: $z = -5.36$, $p < 0.0001$). Comparing both the location and firing rate of these PCs between sessions revealed a coordinated shift across the population, with neurons that shifted their peak location toward the "hotspot" increasing their firing rate and neurons shifting away from it decreasing activity. In control mice, no such shift was detected ([Figure 5E](#)).

Epileptiform-like Discharges Appear During Immobility in CA2-TeTX Mice

Typically, when mice are sleeping or resting quietly, hippocampal LFPs become large and irregular, interspersed with sharp-wave/ripple (SWR) complexes ([Buzsáki, 2015](#)). Recent work has suggested that CA2 PCs may play a role in the initiation of

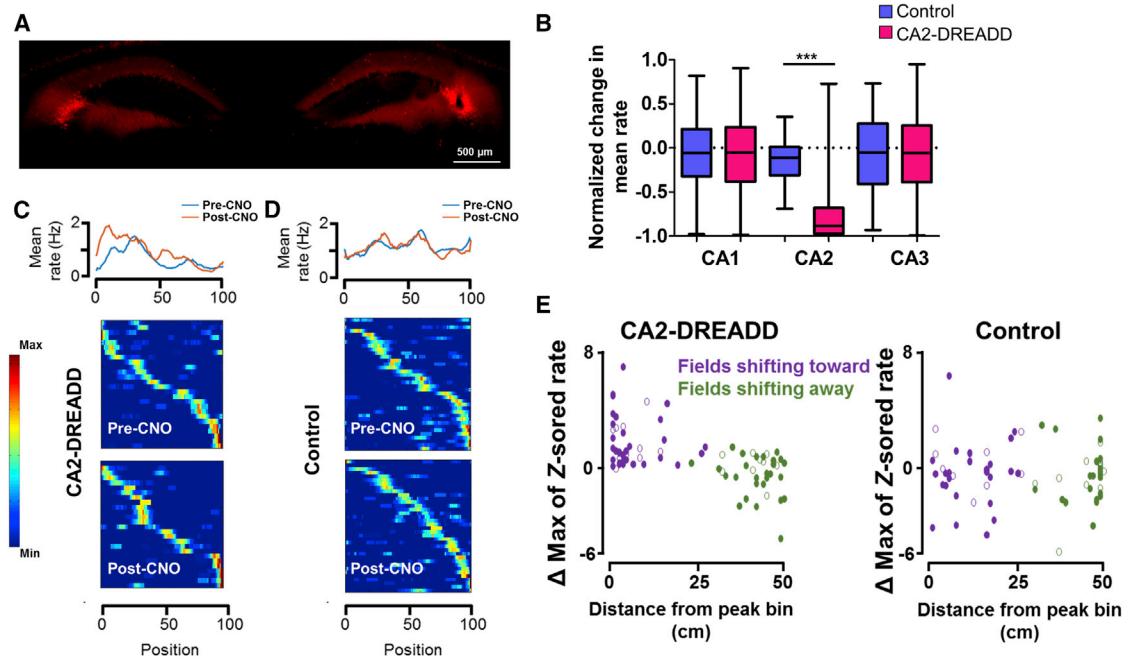


Figure 5. Acute CA2-PC Inhibition Alters the Spatial Distribution of Ensemble Spiking

(A) Bilateral CA2-restricted expression of the G_q -DREADD/mCherry AAV in the CA2-Cre mice. The lesion in the right hemisphere indicates the location of a CA2 targeted tetrode used to monitor CNO-mediated inhibition.

(B) Systemic CNO injection led to a robust inhibition of CA2-PC spiking in the CA2-DREADD mice. Whisker plots show mean value black (line) and min and max range of the normalized change in mean firing rate during the rest period before and after CNO injection. A value of -1 represents complete shutdown of spiking in the post-CNO session.

(C) Example of the spatial distribution of PC ensemble activity from a CA2-DREADD mouse across a linear track recorded before and after CNO injection. At top, spatial distribution of mean firing rate across the entire ensemble ($n = 27$ PCs) is shown in the pre-CNO (blue line) and post-CNO (red line) sessions. CA2 inhibition alters the spatial distribution of the peak rate, leading to the appearance of a new peak in multi-unit activity. Below, the z-scored firing rate map of each PC before (top) and after (bottom) CNO is shown. Cells are aligned by the spatial location of their peak firing rate independently in each session, with warm colors representing high firing and dark colors representing low or zero spikes. In the post-CNO session, there is a concentration of the ensemble representation corresponding to the new multi-unit peak.

(D) Example of the spatial distribution of ensemble activity from a CA2-mCherry control mouse before and after CNO injection. Ensemble rate map is virtually identical between sessions. At top, spatial distribution of mean firing rate across the entire ensemble ($n = 38$ PCs) is shown in the pre-CNO (blue line) and post-CNO (red line) sessions. Below, the z-scored firing rate map of each PC before (top) and after (bottom) CNO is shown, with warm colors representing high firing and dark colors representing low or zero spikes. Cells are aligned by the spatial location of their peak firing rate independently in each session.

(E) Normalized firing-rate change between the pre-CNO and post-CNO run sessions of CA1 and CA3 PCs that demonstrated at least a 10 cm shift in the location of their place field, plotted as a function of their distance from the location of the spatial bin with maximum ensemble activity in the post-CNO session (left, CA2-DREADD, $N = 7$, $n = 158$; right: mCherry, $N = 6$, $n = 149$). In CA2-DREADD mice there is a strong correlation between the proximity to the peak bin and the magnitude and direction of the firing rate change, with neurons that shifted their field toward the peak (purple circles; filled CA1 PCs, open CA3 PCs) increasing their activity and those that shifted away (green circles; filled CA1 PCs, open CA3 PCs) decreasing their activity. No such coordinated relationship is evident in control mice.

See also Table S2 for properties of CA1 and CA3 PCs recorded in control and CA2-DREADD mice.

these SWRs (Oliva et al., 2016a); thus, we next examined the impact of the chronic loss of CA2 output on hippocampal activity during periods of immobility. While we did observe a reduction in the occurrence of normal ripples in the CA2-TeTX mice (control 24.2 ± 1.1 events per min, CA2-TeTX 11.0 ± 1.8 events per min, Mann-Whitney, $p < 0.0001$; Figure 6A), the overall number of high-frequency events was unchanged due to the appearance of epileptiform-like discharges (EDs) similar to those observed in a pre-epileptic state (Wadman et al., 1983). The EDs were large in amplitude (2.14 ± 0.29 mV), short in duration (EDs: 47.5 ± 1.5 ms; control ripples: 106.6 ± 3.0 ms; CA2-TeTX ripples: 110.9 ± 8.1 ms) and occurred with a frequency (2.60 ± 0.22 events per min) consistent with the classic distinction between

normal SWRs and EDs (Buzsáki et al., 1989; Wadman et al., 1983; Figure 6B). Analysis of all CA1 high-frequency events (80–500 Hz) by both their intrinsic frequency and amplitude of the accompanying low-frequency oscillation (1–20 Hz) demonstrated that events were stereotyped in control mice, with little variation. By comparison, multiple populations were evident in CA2-TeTX mice, comprising normal events but additionally high-amplitude, low-frequency events and high-amplitude, high-frequency events (Figure S6). In contrast to SWRs, EDs had a positive polarity in the PC layer, identical to Type II EDs previously described (Buzsáki et al., 1989; Wadman et al., 1983). Simultaneous recordings from CA1 and CA3 ($N = 6$) showed that while the slow-wave component of EDs occurred

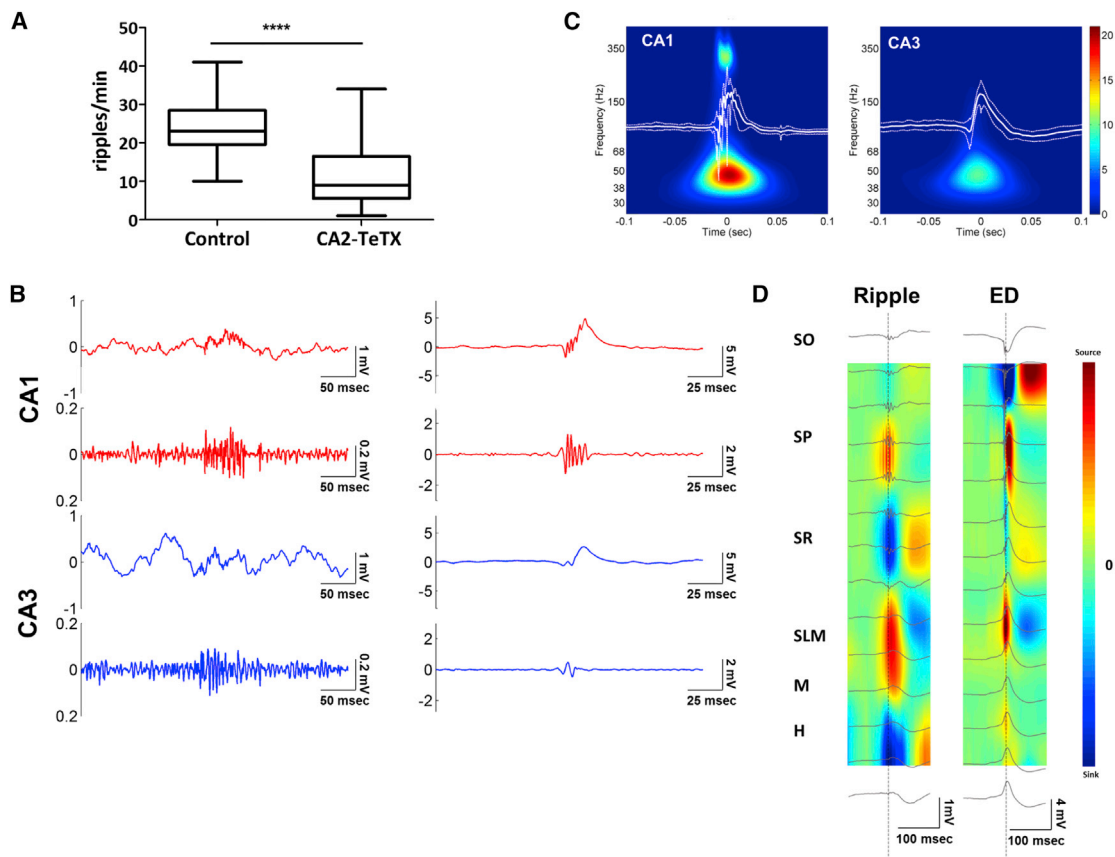


Figure 6. Normal Ripple Events are Replaced with Epileptiform-like Discharges Following CA2 Silencing

(A) The occurrence of normal ripple events detected in CA1 is decreased in the CA2-TeTX mice compared to controls (Mann-Whitney test, $p < 0.001$). Whisker plots show mean value (black line) and min and max range.

(B) On the left, example LFP traces of a normal ripple recorded simultaneously in CA1 (red traces; top trace is the raw LFP, bottom trace is the same data filtered in the 80–300 Hz band) and CA3 (blue traces; top trace is the raw LFP, bottom trace is filtered in the 80–300 Hz band). On the right are LFP traces of an example ED recorded in a CA2-TeTX mouse. Upper red traces are the CA1 raw LFP (top) and LFP filtered in the 80–300 Hz band (bottom), and lower blue traces are the raw (top) and filtered (bottom) LFP simultaneously recorded in CA3. Note the amplitude scale for the ED plots is $5\times$ (raw) or $10\times$ (filtered) larger than the scale of the ripple event, and the temporal scale is reduced by a factor of $0.5\times$ to allow for visualization of the larger, shorter ED events.

(C) Wavelet transform of EDs recorded across a single rest session in the PC layer in CA1 (left) and CA3 (right) reveals a large positive slow component. In CA1, this is accompanied by a high-frequency oscillation. Red represents high power, and blue represents zero power.

(D) Current source density of average ripples (left) and EDs (right) recorded across CA1 in a CA2-TeTX mouse, overlaid with example raw LFP (black). During EDs, there is a positive wave evident in the SR and a corresponding current sink (blue) in the SO. (SO *str. oriens*, SP *str. pyramidale*, SR *str. radiatum*, SLM *str. lacunosum/moleculare*, M *molecular layer of the DG*, H *hilus*).

See also Figure S6.

in both regions, only in CA1 was it accompanied by a high-frequency oscillation (266.6 ± 63.4 Hz; mean \pm SD; Figures 6B and 6C). Further, EDs were observed in CA3 on average 1.98 ± 0.09 ms prior to CA1, suggesting that—similar to SWRs—they were CA3-driven. Finally, to better characterize the inputs driving these events, we implanted a CA2-TeTX mouse with a multi-site linear silicon probe perpendicular to the stratified inputs of CA1 to localize the currents accompanying both normal ripples and EDs. A comparison of current source density (CSD) revealed a prominent current sink in the stratum oriens (SO) during EDs that was distinct from the sink in the stratum radiatum (SR) observed during classic SWRs (Buzsáki, 2015) and consistent with the positive polarity of the EDs recorded in the stratum pyramidale (Figure 6D). Since CA1 basal dendrites in the SO are

preferentially targeted by axons arising from CA2 and CA3a (Ishizuka et al., 1990; Li et al., 1994), and given that CA2 is silenced, our data suggest a mechanism where normal ripples are replaced by EDs due to abnormally strong CA3 input primarily arising in CA3a.

CA2-TeTX Mice Exhibit Slower Contextual Habituation and Susceptibility to Seizure Induction

Previous data have suggested that CA2 may not be critical for spatial and contextual memory (Hitti and Siegelbaum, 2014; Mankin et al., 2015). Indeed, despite the physiological changes we observed, CA2-TeTX mice demonstrated contextual fear memory indistinguishable from controls (Figure S7; control $46.6\% \pm 4.4\%$, CA2-TeTX $46.5\% \pm 7.9\%$, $p = 0.993$). We next

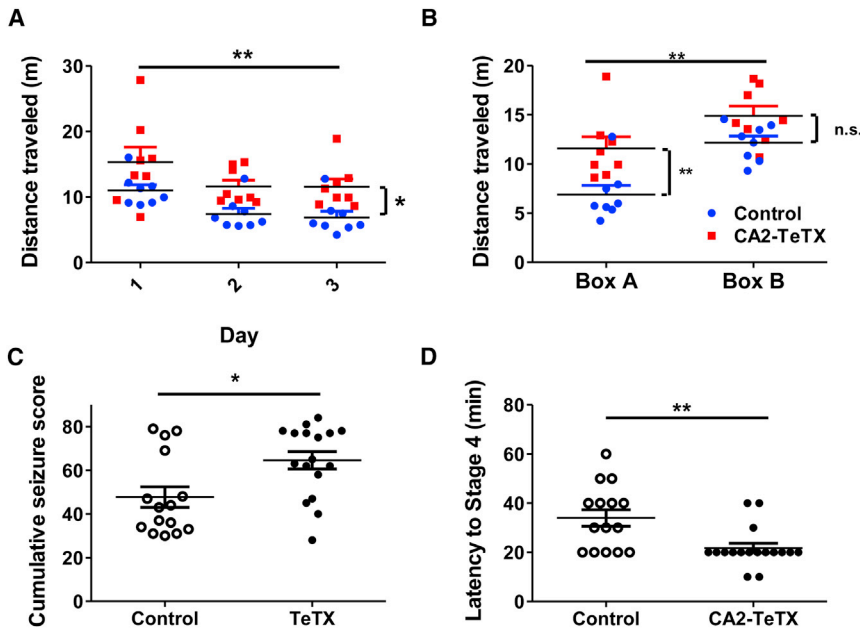


Figure 7. Chronic CA2 Silencing Slows Contextual Learning and Increases Seizure Susceptibility

(A) Contextual habituation is altered in CA2-TeTX mice; average distance traveled across a 5-min exploration session in an open field. On Day 1, the context is novel and induces robust exploration in both CA2-TeTX (red) and control (blue) mice. However, as control mice decrease their exploration across days, locomotion remains high in CA2-TeTX mice, leading to a significant increase on Day 3.

(B) Despite the impairment in habituation, on Day 3 there is no difference in distance traveled between CA2-TeTX (red) and control (blue) mice in a novel context (Box B), suggesting that the difference is not due to general hyperactivity.

(C and D) CA2-TeTX mice demonstrate more severe seizures following systemic injection of kainic acid (KA). Scoring of seizure activity on the modified Racine scale for 2 hr following injection revealed (C) a higher cumulative seizure score and (D) a significantly reduced latency to convulsive seizure. (Mann-Whitney test, * $p < 0.05$, ** $p < 0.01$). All plots show individual subjects and mean \pm SEM. See also Figure S7.

asked whether we could detect more subtle changes in hippocampal-dependent learning by employing a simple context habituation task. In rodents, novel contexts are associated with an initial increase in exploration that decreases both within and between visits as the animal forms a memory of the space (Dixon and Defries, 1968; Halliday, 1966). Although habituation is a complex phenomenon that engages multiple brain systems, it is crucially dependent on the hippocampus, and interventions altering hippocampal memory can delay or eliminate the process (Eichenbaum et al., 1992; Gray and McNaughton, 1983; Wintzer et al., 2014). To examine the relationship between context encoding and CA2 transmission, we habituated CA2-TeTX and control mice to a single context, Box A, for 2 days; on the third day, we exposed them to the familiar context once again, followed by a distinct novel context, Box B. When we compared the total distance traveled by the mice in the familiar box across days, we observed slower habituation in the CA2-TeTX group, with significantly increased exploration evident on day 3 (Figure 7A; two-way repeated-measure ANOVA $F_{2,1}(\text{day} \times \text{virus}) = 0.023$, $p = 0.98$; $F_{2,1}(\text{day}) = 6.94$, $p = 0.004$; $F_{2,1}(\text{virus}) = 13.58$, $p = 0.003$; Bonferroni post-test, Day 3, CA2-TeTX \times control $p < 0.05$). Similar to a previous report, however (Hitti and Siegelbaum, 2014), there was no difference in exploration between CA2-TeTX and control mice in the novel context (Figure 7B; two-way repeated-measure ANOVA $F_{1,1}[\text{box} \times \text{virus}] = 1.02$, $p = 0.33$; $F_{1,1}[\text{box}] = 19.1$, $p = 0.0006$; $F_{1,1}[\text{virus}] = 15.69$, $p = 0.001$; Bonferroni post-test CA2-TeTX \times control: Box A, $p < 0.01$; Box B, $p > 0.05$). Thus, while our data agree that CA2 transmission is dispensable for contextual fear, chronic shutdown slows contextual habituation.

Finally, to address whether the hyperexcitability we observed on the network level increased the susceptibility of CA2-TeTX mice to seizure induction, we injected CA2-TeTX and control mice with the neurotoxin kainic acid (KA) to induce acute sei-

zures. We found that CA2-TeTX mice suffered more severe seizures, with a significant increase in their cumulative seizure score (Figure 7C) and a significant decrease in the latency to convulsion (Figure 7D). These data suggest that while the shift in the E/I balance in the hippocampal circuit resulting from CA2 transmission blockade does not result in spontaneous behavioral seizures, it does predispose the circuit to pathophysiology when challenged.

DISCUSSION

Here we report that a chronic loss of CA2 output leads to increases in excitability in the recurrent CA3 network (Figure 2E) and, more surprisingly, a novel pathophysiology that manifests as hippocampal network hyperexcitability, both during exploration and rest (Figures 3, 4, and 6). While our *in vitro* data suggest that the mechanism underlying these phenotypes is a loss of CA2-PC-driven FFI in CA3, it is important to note that *in vitro* stimulation protocols do not replicate *in vivo* circuit function and may overestimate this process. However, we feel that our ability to detect FFI even at weak stimulation intensities (Figure 1E), coupled with our *in vivo* data implicating increased CA3 circuit excitability as the driver of the pathophysiology (Figure 6D, Table S1), suggest that this inhibition plays a functional role in controlling hippocampal E/I balance. Further, we employed the G_i DREADD system to demonstrate that an acute partial inhibition of CA2-PC spiking led to an increase in the spatial concentration of PC spiking during locomotion, implicating CA2 in preserving a distributed sparse code for place. These observations suggest that CA2 output is necessary to establish the dynamic E/I balance required for proper network function.

One intriguing question is why the place-triggered hyperexcitability events observed in CA2-TeTX mice reflect properties of individual place cells. In both the CA2-TeTX and CA2-DREADD

mice, we observed a subtle but spatially organized shift in PC spiking. In the chronic blockade model, this increase directly preceded the onset of the increase in LFP power (Figure 4B), suggesting a buildup of excitation to levels sufficient to trigger a suprathreshold population event as the underlying cause for the network-wide pathophysiology. Following acute blockade, the increase was less obvious but also spatial in nature; neurons with place fields shifting close to the peak of the ensemble activity increased their firing, while neurons distant from it decreased their firing (Figures 5C and 5D). These findings, combined with the increase in excitability we observed in the recurrent CA3 network (Figure 2E), suggest that one role of CA2-recruited inhibition in CA3 may be to modulate the sparsity and/or strength of CA3 recurrent attractor-state networks. We speculate that the location of the build-up of excitation in a given context may be linked to a pre-existing local maximum in the density of the representation that is reinforced in the absence of CA2-driven inhibition.

A model of an inappropriately strong recurrent CA3 network is also in agreement with the appearance of EDs in the CA2-TeTX mice during immobility (Figures 6B–6D). While the number of ripples decreased in the CA2-TeTX mice (Figure 6A), we feel that our data do not completely agree with the recent suggestion that CA2 PCs may trigger these events (Oliva et al., 2016a). Rather, the decrease in ripples we observed was coincident with the appearance of population spikes similar to those first described in rats that had undergone high-frequency stimulation of CA3 (Wadman et al., 1983). The appearance of the positive EDs during periods of rest in our mice could result from the lack of CA2-mediated inhibition controlling the level of CA3 network activation, suggesting that the activation of CA2 PCs near the onset of ripples may play a role in sculpting the activity of CA3 through both excitation and inhibition. Given the spatial nature of the theta-associated hyperexcitability events observed during behavior, one possibility is that the CA3-driven EDs are related to “replay” events (Wilson and McNaughton, 1994) that include these areas of the context.

A second possible explanation for the spatial nature of the LFP phenotype is related to the shift of CA3 spike timing we observed in the CA2-TeTX mice (Figure 4C). Recent work demonstrated that a CA1 PC receives sufficient spatial information to express a place field at any given location in a context (Lee et al., 2012). What may determine where and when a place field forms is the relative strength and timing of CA3 and EC3 input converging on that cell (Bittner et al., 2015). Specifically, when CA3 and EC3 inputs onto an individual CA1 PC temporally overlap, synaptic plasticity strengthens the CA3 synapses and generates a stable place field at that location (Bittner et al., 2015). Given that a large fraction of the CA3 PCs in the CA2-TeTX mice shift their preference to a phase of theta that would favor this overlap, the place-triggered hyperexcitability (Figures 3 and S3) we observed may reflect a similar mechanism, now simply expressed across a significant portion of the CA1 network.

Given the transient nature of the excitability changes we observed with both chronic and acute CA2 inhibition, an important question is when CA2 mediated FFI is recruited during normal circuit function. It has been demonstrated that inputs from the EC onto CA2 PCs are strong, are highly plastic, and

can lead to rapid and robust output that is temporally coincident with that of the granule cells of the DG (Bartasaghi and Gessi, 2004; Sun et al., 2014). This rapid CA2 response and its recruitment of inhibition in CA3 would allow the EC additional influence on CA3 excitability and favors temporal separation of input from the EC and CA3 onto CA1. Further, the mutually inhibitory nature of the connections between CA2 and CA3, as well as their distinct connectivity along the radial axis of the CA1 PC layer, could allow these two regions to dynamically define distinct states of hippocampal function (Kohara et al., 2014; Valero et al., 2015). This may explain the segregation between the appearance of CA3-driven ripples and CA2-driven, “N-wave” events observed during immobility (Kay et al., 2016). Moreover, inhibition of CA3 PC transmission leads to changes in both rate and temporal coding in CA1 (Middleton and McHugh, 2016), a decrease in the intrinsic frequency of CA1 ripples (Nakashiba et al., 2009), and a resistance to KA seizure induction (Yu et al., 2016). Here we find that CA2-PC silencing leads to a largely opposing set of phenotypes, a pathophysiology similar to that seen in pre-epileptic models (Buzsáki et al., 1989; Wadman et al., 1983), an increase in the frequency and magnitude of fast-oscillations during rest, and an increase in susceptibility to excitotoxic challenge (Figures 7C and 7D). Understanding which EC inputs to CA2 engage this circuit and under what circumstances this occurs will be crucial to further clarifying the role of CA2–CA3 mutual inhibition in normal hippocampal function.

While we see a profound network phenotype following robust and chronic CA2 blockade in the CA2-TeTX mice, the phenotype in the acutely inhibited CA2-DREADD mice is comparatively subtle. Whether these differences are due to the difference in the degree of transmission inhibition between the two approaches and/or a consequence of acute versus chronic silencing is difficult to determine. In the CA2-DREADD mice, we have the ability to quantify the degree of neuronal inhibition in vivo via tetrodes placed in CA2. We found average spike rates of CA2 PCs following CNO administration to be reduced by about 75% (Figure 5B), which is in line with previous reports in the entorhinal cortex (Miao et al., 2015). This partial inhibition is in contrast to the virtually complete blockade of CA2 output observed in slices from CA2-TeTX mice (Figure 2C). All the CA2-TeTX mice included in this study had robust, bilateral expression of the virus across the dorsal CA2 (Figure 2A, Figure S1). We did record from two additional mice, not included in the dataset, in which there was no expression in the hemisphere contralateral to our recording site due to mistargeted injections. Interestingly, neither of these unilaterally expressing mice exhibited the phenotypes we observed in bilaterally expressing animals, suggesting that a complete silencing of the circuit, which has strong contralateral projections, is necessary. Recent literature has made it clear that it is common to find discrepancies between the effects of transient and chronic manipulations on neuronal activity for a variety of reasons. However, compensation for the loss of output in the brain has repeatedly been shown to correct for imbalances in inhibition and excitation on the circuit level, not magnify them (Otchy et al., 2015). Thus, we speculate that the pathophysiology we observed in the CA2-TeTX mouse is not an artifact of non-specific compensation; rather, it represents the cumulative impact of complete long-term loss of dorsal

CA2 transmission. While partial or transient manipulations may be unable to replicate the full phenotype, we did observe similarities at the single-cell level.

Previous behavioral characterization of a similar CA2-TeTX mouse model reported no significant changes in contextual or spatial learning (Hitti and Siegelbaum, 2014). In our mice, we observed a significant decrease in the spatial specificity of both CA1 and CA3 place cells; nonetheless, our mice could be conditioned to fear a novel context, in agreement with the previous report. However, when we examined contextual habituation (Wintzer et al., 2014), we found the CA2-TeTX mice demonstrated a prolonged novelty response despite repeated presentations of the same context. It is difficult to speculate on the direct relationship between the physiology and behavior, as we do not know what constitutes a spatial representation that is “good enough” to support fear conditioning, but not behavioral habituation. However, these data suggest that CA2 transmission does play a role in spatial learning, perhaps through its influence on overall network excitability. An additional question not specifically addressed here is what the contribution may be of the descending projections from CA2 PCs to both the medial septum (MS) and supramammillary nucleus (SuM) (Cui et al., 2013), two areas critical for the regulation of the theta oscillation. Manipulations of ascending projections from the MS to the hippocampus have been shown to alter both theta oscillations and locomotion in a cell-type-specific and pathway-specific manner (Bender et al., 2015; Fuhrmann et al., 2015; Robinson et al., 2016); however, neither the post-synaptic targets of the CA2 axons in the MS (GABAergic, glutamatergic, and/or cholinergic neurons) nor the physiological consequences of transmission in this descending CA2 pathway have been identified. Thus, it is difficult to speculate on the link between CA2 synaptic silencing and these earlier results. Future work specifically dissecting these projections may elucidate the hippocampal and subcortical contributions to the pathophysiology associated with a loss of CA2 transmission.

In conclusion, our data demonstrate profound effects of CA2 silencing on both the single-neuron and network level, both “downstream” in CA1 and “upstream” in CA3. Moreover, we find a novel pathophysiology that manifests as spatially triggered hyperexcitability. We believe that our findings suggest a key role of CA2 transmission in the dynamic regulation of information flow in the hippocampal circuit.

STAR★METHODS

Detailed methods are provided in the online version of this paper and include the following:

- [KEY RESOURCES TABLE](#)
- [CONTACT FOR REAGENT AND RESOURCE SHARING](#)
- [EXPERIMENTAL MODEL AND SUBJECT DETAILS](#)
 - Subjects
 - Generation of the Cacng5-Cre Mouse Line
 - Adeno-Associated Virus Vector Construction
 - AAV Production
- [METHOD DETAILS](#)
 - Immunohistochemistry

- [In Vivo Electrophysiology](#)
- [In Vitro Electrophysiology](#)
- [Mouse Behavior](#)
- [QUANTIFICATION AND STATISTICAL ANALYSIS](#)
 - [In Vivo Electrophysiology](#)
- [STATISTICS](#)
- [DATA AND SOFTWARE AVAILABILITY](#)

SUPPLEMENTAL INFORMATION

Supplemental Information includes seven figures, two tables, and one movie and can be found with this article online at <http://dx.doi.org/10.1016/j.neuron.2017.04.014>.

AUTHOR CONTRIBUTIONS

T.J.M., R.B., R.A.P., and V.C. designed experiments. R.B., V.R., R.A.P., V.C., S.J.M., M.E.W., and T.J.M. conducted experiments. R.B., D.P., S.J.M., R.A.P., V.C., and T.J.M. performed data analyses. A.J.Y.H. generated reagents. T.J.M. wrote the manuscript with input from all authors.

ACKNOWLEDGMENTS

We would like to thank all CBP members for help and support, Hongshen He for input on analyses, and Drs. Hajime Hirase and Charles Yokoyama for comments on the manuscript. We thank Ludivine Therreau for technical support, Dr. Kenji Yamazawa and the Advanced Manufacturing Support Team of the RIKEN Center for Advanced Photonics for assistance in microdrive production, and the RIKEN BSI RRC for transgenic production. This work was supported by the RIKEN Brain Science Institute (T.J.M.).

Received: April 22, 2016

Revised: February 16, 2017

Accepted: April 6, 2017

Published: May 3, 2017

REFERENCES

- Agarwal, G., Stevenson, I.H., Berényi, A., Mizuseki, K., Buzsáki, G., and Sommer, F.T. (2014). Spatially distributed local fields in the hippocampus encode rat position. *Science* *344*, 626–630.
- Ahmed, O.J., and Mehta, M.R. (2009). The hippocampal rate code: anatomy, physiology and theory. *Trends Neurosci.* *32*, 329–338.
- Alexander, G.M., Farris, S., Pirone, J.R., Zheng, C., Colgin, L.L., and Dudek, S.M. (2016). Social and novel contexts modify hippocampal CA2 representations of space. *Nat. Commun.* *7*, 10300.
- Ambruster, B.N., Li, X., Pausch, M.H., Herlitze, S., and Roth, B.L. (2007). Evolving the lock to fit the key to create a family of G protein-coupled receptors potentially activated by an inert ligand. *Proc. Natl. Acad. Sci. USA* *104*, 5163–5168.
- Bartasaghi, R., and Gessi, T. (2004). Parallel activation of field CA2 and dentate gyrus by synaptically elicited perforant path volleys. *Hippocampus* *14*, 948–963.
- Bender, F., Gorbati, M., Cadavieco, M.C., Denisova, N., Gao, X., Holman, C., Korotkova, T., and Ponomarenko, A. (2015). Theta oscillations regulate the speed of locomotion via a hippocampus to lateral septum pathway. *Nat. Commun.* *6*, 8521.
- Berens, P. (2009). CircStat: a MATLAB toolbox for circular statistics. *J. Stat. Softw.* *31*, 1–21.
- Bittner, K.C., Grienberger, C., Vaidya, S.P., Milstein, A.D., Macklin, J.J., Suh, J., Tonegawa, S., and Magee, J.C. (2015). Conjunctive input processing drives feature selectivity in hippocampal CA1 neurons. *Nat. Neurosci.* *18*, 1133–1142.

- Boccarda, C.N., Kjonigsen, L.J., Hammer, I.M., Bjaalie, J.G., Leergaard, T.B., and Witter, M.P. (2015). A three-plane architectonic atlas of the rat hippocampal region. *Hippocampus* 25, 838–857.
- Buzsáki, G. (2015). Hippocampal sharp wave-ripple: a cognitive biomarker for episodic memory and planning. *Hippocampus* 25, 1073–1188.
- Buzsáki, G., Ponomareff, G.L., Bayardo, F., Ruiz, R., and Gage, F.H. (1989). Neuronal activity in the subcortically denervated hippocampus: a chronic model for epilepsy. *Neuroscience* 28, 527–538.
- Chevalyere, V., and Siegelbaum, S.A. (2010). Strong CA2 pyramidal neuron synapses define a powerful disinhibitory cortico-hippocampal loop. *Neuron* 66, 560–572.
- Csicsvari, J., Hirase, H., Czurkó, A., Mamiya, A., and Buzsáki, G. (1999). Fast network oscillations in the hippocampal CA1 region of the behaving rat. *J. Neurosci.* 19, RC20.
- Cui, Z., Gerfen, C.R., and Young, W.S., 3rd (2013). Hypothalamic and other connections with dorsal CA2 area of the mouse hippocampus. *J. Comp. Neurol.* 521, 1844–1866.
- Czurkó, A., Hirase, H., Csicsvari, J., and Buzsáki, G. (1999). Sustained activation of hippocampal pyramidal cells by ‘space clamping’ in a running wheel. *Eur. J. Neurosci.* 11, 344–352.
- Delorme, A., and Makeig, S. (2004). EEGLAB: an open source toolbox for analysis of single-trial EEG dynamics including independent component analysis. *J. Neurosci. Methods* 134, 9–21.
- Dixon, L.K., and Defries, J.C. (1968). Development of open-field behavior in mice. *Dev. Psychobiol.* 1, 100–107.
- Dudek, S.M., Alexander, G.M., and Farris, S. (2016). Rediscovering area CA2: unique properties and functions. *Nat. Rev. Neurosci.* 17, 89–102.
- Eichenbaum, H., Otto, T., and Cohen, N.J. (1992). The hippocampus—what does it do? *Behav. Neural Biol.* 57, 2–36.
- Fuhrmann, F., Justus, D., Sosulina, L., Kaneko, H., Beutel, T., Friedrichs, D., Schoch, S., Schwarz, M.K., Fuhrmann, M., and Remy, S. (2015). Locomotion, theta oscillations, and the speed-correlated firing of hippocampal neurons are controlled by a medial septal glutamatergic circuit. *Neuron* 86, 1253–1264.
- Gray, J.A., and McNaughton, N. (1983). Comparison between the behavioural effects of septal and hippocampal lesions: a review. *Neurosci. Biobehav. Rev.* 7, 119–188.
- Halliday, M.S. (1966). Effect of previous exploratory activity on the exploration of a simple maze. *Nature* 209, 432–433.
- Hitti, F.L., and Siegelbaum, S.A. (2014). The hippocampal CA2 region is essential for social memory. *Nature* 508, 88–92.
- Ishizuka, N., Weber, J., and Amaral, D.G. (1990). Organization of intrahippocampal projections originating from CA3 pyramidal cells in the rat. *J. Comp. Neurol.* 295, 580–623.
- Jones, M.W., and McHugh, T.J. (2011). Updating hippocampal representations: CA2 joins the circuit. *Trends Neurosci.* 34, 526–535.
- Kay, K., Sosa, M., Chung, J.E., Karlsson, M.P., Larkin, M.C., and Frank, L.M. (2016). A hippocampal network for spatial coding during immobility and sleep. *Nature* 531, 185–190.
- Kim, J.H., Lee, S.R., Li, L.H., Park, H.J., Park, J.H., Lee, K.Y., Kim, M.K., Shin, B.A., and Choi, S.Y. (2011). High cleavage efficiency of a 2A peptide derived from porcine teschovirus-1 in human cell lines, zebrafish and mice. *PLoS ONE* 6, e18556.
- Kohara, K., Pignatelli, M., Rivest, A.J., Jung, H.Y., Kitamura, T., Suh, J., Frank, D., Kajikawa, K., Mise, N., Obata, Y., et al. (2014). Cell type-specific genetic and optogenetic tools reveal hippocampal CA2 circuits. *Nat. Neurosci.* 17, 269–279.
- Krashes, M.J., Koda, S., Ye, C., Rogan, S.C., Adams, A.C., Cusher, D.S., Maratos-Flier, E., Roth, B.L., and Lowell, B.B. (2011). Rapid, reversible activation of AgRP neurons drives feeding behavior in mice. *J. Clin. Invest.* 121, 1424–1428.
- Lee, D., Lin, B.J., and Lee, A.K. (2012). Hippocampal place fields emerge upon single-cell manipulation of excitability during behavior. *Science* 337, 849–853.
- Lee, H., Wang, C., Deshmukh, S.S., and Knierim, J.J. (2015). Neural population evidence of functional heterogeneity along the CA3 transverse axis: pattern completion versus pattern separation. *Neuron* 87, 1093–1105.
- Li, X.G., Somogyi, P., Ylinen, A., and Buzsáki, G. (1994). The hippocampal CA3 network: an in vivo intracellular labeling study. *J. Comp. Neurol.* 339, 181–208.
- Lorente de No, R. (1934). Studies on the structure of the cerebral cortex. II. Continuation of the study of the ammonic system. *J. Psychol. Neurol.* 46, 113–177.
- Lu, L., Igarashi, K.M., Witter, M.P., Moser, E.I., and Moser, M.B. (2015). Topography of place maps along the CA3-to-CA2 axis of the hippocampus. *Neuron* 87, 1078–1092.
- Mankin, E.A., Diehl, G.W., Sparks, F.T., Leutgeb, S., and Leutgeb, J.K. (2015). Hippocampal CA2 activity patterns change over time to a larger extent than between spatial contexts. *Neuron* 85, 190–201.
- McHugh, T.J., Blum, K.I., Tsien, J.Z., Tonegawa, S., and Wilson, M.A. (1996). Impaired hippocampal representation of space in CA1-specific NMDAR1 knockout mice. *Cell* 87, 1339–1349.
- McHugh, T.J., Jones, M.W., Quinn, J.J., Balthasar, N., Coppari, R., Elmquist, J.K., Lowell, B.B., Fanselow, M.S., Wilson, M.A., and Tonegawa, S. (2007). Dentate gyrus NMDA receptors mediate rapid pattern separation in the hippocampal network. *Science* 317, 94–99.
- Miao, C., Cao, Q., Ito, H.T., Yamahachi, H., Witter, M.P., Moser, M.B., and Moser, E.I. (2015). Hippocampal remapping after partial inactivation of the medial entorhinal cortex. *Neuron* 88, 590–603.
- Middleton, S.J., and McHugh, T.J. (2016). Silencing CA3 disrupts temporal coding in the CA1 ensemble. *Nat. Neurosci.* 19, 945–951.
- Mitra, P., and Bokil, H. (2008). *Observed Brain Dynamics* (Oxford University Press).
- Moser, E.I., Kropff, E., and Moser, M.B. (2008). Place cells, grid cells, and the brain’s spatial representation system. *Annu. Rev. Neurosci.* 31, 69–89.
- Nakashiba, T., Young, J.Z., McHugh, T.J., Buhl, D.L., and Tonegawa, S. (2008). Transgenic inhibition of synaptic transmission reveals role of CA3 output in hippocampal learning. *Science* 319, 1260–1264.
- Nakashiba, T., Buhl, D.L., McHugh, T.J., and Tonegawa, S. (2009). Hippocampal CA3 output is crucial for ripple-associated reactivation and consolidation of memory. *Neuron* 62, 781–787.
- Oliva, A., Fernández-Ruiz, A., Buzsáki, G., and Berényi, A. (2016a). Role of hippocampal CA2 region in triggering sharp-wave ripples. *Neuron* 91, 1342–1355.
- Oliva, A., Fernández-Ruiz, A., Buzsáki, G., and Berényi, A. (2016b). Spatial coding and physiological properties of hippocampal neurons in the Cornu Ammonis subregions. *Hippocampus* 26, 1593–1607.
- Otchy, T.M., Wolff, S.B., Rhee, J.Y., Pehevian, C., Kawai, R., Kempf, A., Gobes, S.M., and Ölveczky, B.P. (2015). Acute off-target effects of neural circuit manipulations. *Nature* 528, 358–363.
- Pearce, P.S., Friedman, D., Lafrancois, J.J., Iyengar, S.S., Fenton, A.A., Macluskay, N.J., and Scharfman, H.E. (2014). Spike-wave discharges in adult Sprague-Dawley rats and their implications for animal models of temporal lobe epilepsy. *Epilepsy Behav.* 32, 121–131.
- Racine, R.J. (1972). Modification of seizure activity by electrical stimulation. II. Motor seizure. *Electroencephalogr. Clin. Neurophysiol.* 32, 281–294.
- Robinson, J., Manseau, F., Ducharme, G., Amihon, B., Vigneault, E., El Mestikawy, S., and Williams, S. (2016). Optogenetic activation of septal glutamatergic neurons drive hippocampal theta rhythms. *J. Neurosci.* 36, 3016–3023.
- Rowland, D.C., Weible, A.P., Wickersham, I.R., Wu, H., Mayford, M., Witter, M.P., and Kentros, C.G. (2013). Transgenically targeted rabies virus demonstrates a major monosynaptic projection from hippocampal area CA2 to medial entorhinal layer II neurons. *J. Neurosci.* 33, 14889–14898.
- Royer, S., Zemelman, B.V., Losonczy, A., Kim, J., Chance, F., Magee, J.C., and Buzsáki, G. (2012). Control of timing, rate and bursts of hippocampal place cells by dendritic and somatic inhibition. *Nat. Neurosci.* 15, 769–775.

- Schmitzer-Torbert, N., Jackson, J., Henze, D., Harris, K., and Redish, A.D. (2005). Quantitative measures of cluster quality for use in extracellular recordings. *Neuroscience* 131, 1–11.
- Sekino, Y., Obata, K., Tanifuji, M., Mizuno, M., and Murayama, J. (1997). Delayed signal propagation via CA2 in rat hippocampal slices revealed by optical recording. *J. Neurophysiol.* 78, 1662–1668.
- Siapas, A.G., Lubenov, E.V., and Wilson, M.A. (2005). Prefrontal phase locking to hippocampal theta oscillations. *Neuron* 46, 141–151.
- Skaggs, W.E., McNaughton, B.L., and Gothard, K.M. (1993). An information-theoretic approach to deciphering the hippocampal code. *Proceedings of Advances in Neural Processing Systems* 5, 1030–1037.
- Squire, L.R., Stark, C.E., and Clark, R.E. (2004). The medial temporal lobe. *Annu. Rev. Neurosci.* 27, 279–306.
- Sun, Q., Srinivas, K.V., Sotayo, A., and Siegelbaum, S.A. (2014). Dendritic Na(+) spikes enable cortical input to drive action potential output from hippocampal CA2 pyramidal neurons. *eLife* 3, 04551.
- Torrence, C., and Compo, G.P. (1998). A practical guide to wavelet analysis. *Bull. Am. Meteorol. Soc.* 79, 61–78.
- Valero, M., Cid, E., Averkin, R.G., Aguilar, J., Sanchez-Aguilera, A., Viney, T.J., Gomez-Dominguez, D., Bellistri, E., and de la Prida, L.M. (2015). Determinants of different deep and superficial CA1 pyramidal cell dynamics during sharp-wave ripples. *Nat. Neurosci.* 18, 1281–1290.
- Wadman, W.J., Da Silva, F.H., and Leung, L.W. (1983). Two types of interictal transients of reversed polarity in rat hippocampus during kindling. *Electroencephalogr. Clin. Neurophysiol.* 55, 314–319.
- Wilson, M.A., and McNaughton, B.L. (1994). Reactivation of hippocampal ensemble memories during sleep. *Science* 265, 676–679.
- Wintzer, M.E., Boehringer, R., Polygalov, D., and McHugh, T.J. (2014). The hippocampal CA2 ensemble is sensitive to contextual change. *J. Neurosci.* 34, 3056–3066.
- Yu, L.M.Y., Polygalov, D., Wintzer, M.E., Chiang, M.-C., and McHugh, T.J. (2016). CA3 synaptic silencing attenuates kainic acid-induced seizures and hippocampal network oscillations. *eNeuro* 3.

STAR★METHODS

KEY RESOURCES TABLE

REAGENT or RESOURCE	SOURCE	IDENTIFIER
Antibodies		
Mouse α -GAD67	Millipore	Cat# MAB5406; RRID: AB_2278725
Alexa Fluor 594-conjugated donkey α -mouse	Thermo Fisher	Cat# A-21203; RRID: AB_2535789
Mouse α -Cre	Millipore	Cat# MAB3120; RRID: AB_2085748
Rabbit α -PCP4	Santa Cruz Biotechnology	Cat# sc-74816; RRID: AB_2236566
Alexa Fluor 488-conjugated donkey α -mouse	Thermo Fisher	Cat# A-21202; RRID: AB_2535788
Alexa Fluor 594-conjugated donkey α -rabbit	Thermo Fisher	Cat# A21207; RRID: AB_141637
Bacterial and Virus Strains		
Stb3 Chemically Competent Cells	Thermo Fisher	Cat# C737303
AAV.EF1a.DIO.mCherry	This paper	N/A
AAV.EF1a.DIO.TeTX.2A.mCherry	This paper	N/A
AAV.CaMKII.DIO.TeTX.2A.mCherry	This paper	N/A
AAV.EF1a.DIO.hChR2(H134R).EYFP	This paper	N/A
AAV.hSyn.DIO.hM4D.Gi.mCherry	This paper	N/A
Chemicals, Peptides, and Recombinant Proteins		
Clozapine-N-oxide	Sigma	SKU: C0832; CAS Number: 34233-97-7
Kainic acid	Sigma	Cat#: K0250; CAS Number 58002-62-3
SR 95531 hydrobromide	Tocris	Cat#: 1262; CAS Number: 104104-50-9
CGP 55845 hydrochloride	Tocris	Cat#: 1248; CAS Number: 149184-22-5
Critical Commercial Assays		
ProLong Gold	Thermo Fisher	Cat#: P36930
VECTASHIELD Mounting Medium with DAPI	Vector Laboratories	Cat#: H-1500; RRID AB_2336788
Quick & Easy BAC Modification Kit	GeneBridges (GmbH)	Cat#: K001
QIAGEN Large Construct Kit	QIAGEN	Cat#: 12462
293fectin	Invitrogen	Cat#: 12347-019
FastStart Universal SYBR Green Master	Roche	Cat#: 04673484001
Experimental Models: Cell Lines		
293FT cell line	Thermo Fisher	Cat#: R700-07
Experimental Models: Organisms/Strains		
Mouse: C57BL6/J-Cacng5-Cre	This paper	N/A
Oligonucleotides		
Primers (5' → 3')		
TGCTCCTTTTACGCTATGTGG	Invitrogen	WPRE.QPCR.f
ATAAAGAGACAGCAACCAGG	Invitrogen	WPRE.QPCR.r
aaacccaagctagccaccatggtgagcaagggcgag gaggataaca	Invitrogen	mCherry.Nhe.f
aaacccaagggcgcgcttactgtacagctcgcca	Invitrogen	mCherry.Asc.r
TTTGGGTTTGCTAGCCACCATGCCAATAA CCATAAATAATTTTAGATATAGTG	Invitrogen	TeNT.Nhe.f
TTTGGGTTTGCGGCCGCTGCAGTTCTATT ATATAAATTTCTCTT	Invitrogen	TeNT.Not.r

(Continued on next page)

Continued

REAGENT or RESOURCE	SOURCE	IDENTIFIER
TTTGGGTTTGCGGCCGCCACCAAGAAGAA ACAGAAAATTGTGGCACCAGTGAAACAG	Invitrogen	2A.Not.f
TTTGGGTTTGCGGCCGCCCTATTACTTGTA CAGCTCGTCCATGCCGCCGGT	Invitrogen	mCherry.Asc.r
Recombinant DNA		
pAAV.EF1a.DIO.mCherry	This paper	N/A
pAAV.EF1a.DIO.TeTX.2A.mCherry	This paper	N/A
pAAV.CaMKII.DIO.TeTX.2A.mCherry	This paper	N/A
pAAV.EF1a.DIO.hChR2(H134R).EYFP	Deisseroth Lab (Stanford University)	N/A
pAAV.hSyn.DIO.hM4D.Gi.mCherry	Krashes et al., 2011	Addgene plasmid #44362
pAAV-DJ/8	Cell Biolabs	Cat#: VPK-420-DJ-8
pHelper	Agilent Technologies	Cat#: 240071
Software and Algorithms		
MATLAB R2009b	MathWorks	https://www.mathworks.com/products/matlab
Prism v5.04	GraphPad	http://www.graphpad.com/
SpikeSort 3D v2.5.1.0	NeuraLynx	http://neuralynx.com/research_software/spike_sort_3d
Axograph X	Axograph	http://www.axographx.com/
pClamp10	Molecular Devices	https://www.moleculardevices.com/systems/conventional-patch-clamp/pclamp-10-software
FreezeFrame v3.082	Actimetrics	http://actimetrics.com
FreezeView v3.08	Actimetrics	http://actimetrics.com
ANY-maze v4.84	Stoelting	http://www.anymaze.co.uk/
Cheetah v5.6.0	NeuraLynx	http://neuralynx.com/
EventSessionSplitter v.2.1.2	NeuraLynx	http://neuralynx.com/
Wavelet analysis	Torrence and Compo, 1998	http://paos.colorado.edu/research/wavelets/
CircStat: A MATLAB Toolbox for Circular Statistics	P. Berens	http://bethgelab.org/software/circstat/
Chronux Toolbox v 2.11	Mitra and Bokil, 2008	http://chronux.org/

CONTACT FOR REAGENT AND RESOURCE SHARING

Further information and requests for resources and reagents should be directed to and will be fulfilled by the Lead Contact, Dr. Thomas McHugh (tjmchugh@brain.riken.jp).

EXPERIMENTAL MODEL AND SUBJECT DETAILS**Subjects**

All procedures were approved by the RIKEN Animal Care and Use Committee and/or in accordance with the regulations the animal care committee of the Université Paris Descartes. All experiments were conducted with male mice hemizygous for the *Cacng5-Cre* transgene (age 1.5-5 months) injected with Cre-dependent AAV virus or viruses into CA2 as described in the experimental methods. The mice were housed in transparent Plexiglas cages placed in ventilated racks and maintained in a temperature- and humidity-controlled room with a 12-h light/dark cycle cycle (lights on from 08:00 to 20:00). Prior to stereotaxic surgery all animals were housed in groups of 2 to 5 and provided with food and water ad libitum. Animals implanted with microdrives or linear probes were single housed following surgery. Prior to in vivo and in vitro electrophysiology experiments the animals were experimentally naive and randomly assigned in respect to which virus or viruses were injected. All mice used for behavioral experiments were randomly assigned to receive TeTX or control mCherry virus and had previously not been used for any experiments. All experiments were conducted during the animals' light cycle.

Generation of the *Cacng5-Cre* Mouse Line

The bacterial artificial chromosome (BAC) RP23-145G23 (BACPAC Resources Center) containing the calcium channel, voltage-dependent, gamma subunit 5 (*cacng5*) was modified using the Quick & Easy BAC Modification Kit (Gene Bridges GmbH) to insert

a Cre-FRT-Amp-FRT cassette at the start site of *cacng5* translation. The ampicillin (Amp) marker was deleted utilizing Flp-706 recombination and the Cre-modified BAC's were confirmed by PCR analysis. The confirmed Cre-modified RP23-145G23 BAC was subsequently purified using the QIAGEN Large Construct Kit (QIAGEN). To prepare the modified BAC for microinjection, 50 μ g of Cre-modified RP23-145G23 BAC was linearized using *AscI* (New England Biolabs) and then buffer exchanged using the Sepharose CL-4B matrix (Pharmacia/Pfizer) into an injection buffer composed of 10 mM Tris-HCl, pH7.4, 0.1 mM EDTA, and 100 mM NaCl. The purified BAC was injected into C57BL/6 fertilized pronuclei and fertilized blastocysts were implanted into pseudopregnant females. From the microinjections, five *Cacng5-Cre* B6 founders (lines 160, 181, 190, 212, 225) were generated. The 181 *Cacng5-Cre* line was determined to express Cre selectively in the CA2 area of hippocampus using immunohistochemistry with the α Cre antibody (Millipore, MAB 3120). The 181 line was maintained in a pure C57BL/6 background in a specific-pathogen-free animal facility and male mice between the ages of 2 and 5 months were used for all experiments.

Adeno-Associated Virus Vector Construction

The pAAV.hSyn.DIO.hM4D.Gi.mCherry plasmid was a gift from Bryan Roth (Addgene plasmid # 44362). The pAAV.DIO.hChR2(H134R).EYFP plasmid was a gift from Karl Deisseroth (Stanford University).

The recombinant Adeno-Associated Virus (AAV) vectors pAAV.EF1a.DIO.mCherry, pAAV.EF1a.DIO.TeTX.2A.mCherry, and pAAV.CaMKII.DIO.TeTX.2A.mCherry were generated within our laboratory. For the construction of pAAV.EF1a.DIO.mCherry, the mCherry DNA fragment was generated using the high fidelity Phusion DNA Polymerase (NEB). At the 5' end of the DNA fragment, the *NheI* restriction enzyme site is followed by latter half of the Kozak sequence (CACC) for translational efficiency and then the ATG start codon for mCherry. The 3' end of the mCherry DNA fragment contains the *AscI* restriction enzyme site preceded by two tandem stop codons. The PCR-generated cassette was digested with *NheI* (NEB) and *AscI* (NEB). The vector backbone for this construct was the pAAV.EF1a.DIO.hChR2(H134R).EYFP plasmid (Deisseroth lab) digested with *NheI* and *AscI* and treated with calf intestine phosphate (NEB). The approximately 5.5 kB DNA fragment containing the vector backbone was ligated to the digested mCherry DNA fragment with T4 DNA ligase buffer (NEB) and transformed into One Shot Stbl3 Chemically Competent Cells (Invitrogen) and colonies were screened by restriction digest analysis. The putative positive colonies were submitted for DNA sequencing and one clone with the correct DNA sequence was designated as pAAV.EF1a.DIO.mCherry.

For the construction of pAAV.EF1a.DIO.TeTX.2A.mCherry, the TeTX.2A and mCherry DNA fragments was generated using high-fidelity PCR as described above. The 5' end of the TeTX.2A cassette is composed of the *NheI* restriction enzyme site, followed by the latter half of the Kozak sequence and then the ATG start codon for tetanus toxin light chain (TeTX). The 3' end of the TeTX.2A cassette contains the *PspOMI* restriction enzyme site preceded by the sequence for p2A generated from the published sequence (Kim et al., 2011) and then preceded by a portion of the 3' open reading frame (ORF) for TeTX. At the 5' end of the mCherry cassette, the *PspOMI* restriction enzyme site is followed by the in-frame sequence of the mCherry gene without the ATG start codon. The 3' end of the mCherry cassette contains the *AscI* restriction enzyme site preceded by two tandem stop codons. The PCR-generated TeTX.2A cassette was digested with *NheI* (NEB) and *PspOMI* (NEB) while the PCR-generated mCherry cassette was digested with *PspOMI* (NEB) and *AscI* (NEB). The vector backbone for this construct was the pAAV.EF1a.DIO.hChR2(H134R).EYFP plasmid (Deisseroth lab) digested with *NheI* and *AscI* and treated with calf intestine phosphate (NEB). The approximately 5.5 kB DNA fragment containing the vector backbone was ligated to the digested TeTX.2A and mCherry DNA fragments with T4 DNA ligase buffer (NEB) and transformed into One Shot Stbl3 Chemically Competent Cells (Invitrogen) and colonies were screened by restriction digest analysis. The putative positive colonies were submitted for DNA sequencing and one clone with the correct DNA sequence was designated as pAAV.EF1a.DIO.TeTX.2A.mCherry.

For the construction of pAAV.CaMKII.DIO.TeTX.2A.mCherry, the CaMKII promoter DNA fragments was generated using the high-fidelity PCR as described above. At the 5' end of the DNA fragment, the *MluI* (NEB) restriction enzyme site is followed by 5' end of the CaMKII promoter sequence. The 3' end of the DNA fragment contains the *BamHI* (NEB) restriction enzyme site preceded by two tandem stop codons. The PCR-generated cassette was digested with *MluI* (NEB) and *BamHI* (NEB). The vector backbone for this construct was the pAAV.EF1a.DIO.TeTX.2A.mCherry plasmid, described above, digested with *MluI* and *BamHI* and treated with calf intestine phosphate (NEB). The approximately 6.5 kB DNA fragment containing the vector backbone was ligated to the digested CaMKII promoter DNA fragment with T4 DNA ligase buffer (NEB) and transformed into One Shot Stbl3 Chemically Competent Cells (Invitrogen) and colonies were screened by restriction digest analysis. The putative positive colonies were submitted for DNA sequencing and one clone with the correct DNA sequence was designated as pAAV.CaMKII.DIO.TeTX.2A.mCherry.

AAV Production

For adeno-associated virus production, we used the AAV Helper Free System (Agilent Technologies). The adeno-associated virus vector (pAAV.EF1a.DIO.mCherry, pAAV.EF1a.DIO.hChR2(H134R).EYFP, pAAV.EF1a.DIO.TeTX2A.mCherry, pAAV.hSyn.DIO.hM4D.Gi.mCherry, or pAAV.CaMKII.DIO.TeTX2A.mCherry) was co-transfected with pAAV-DJ/8 (Cell Biolabs), which supplies AAV2 replication proteins and AAV-DJ/8 capsid proteins, and pHelper (Agilent Technologies), which supplies the necessary adeno-virus gene products required for the AAV production into the 293FT cell line (Invitrogen) utilizing the 293fectin transfection reagent (Invitrogen). After 72 hr, the supernatant was collected and centrifuged at 3,000 rpm for 30 min and then filtered through a 0.45 μ m filtration unit (Millipore). Purification of the AAV was carried out by ultracentrifugation (87,000 g, 4°C, 2 h) with a 20% sucrose cushion. After ultracentrifugation, the supernatant was removed and the pellet was resuspended in phosphate-buffered saline (PBS),

aliquoted and stored at -80°C for long term storage. The AAV stocks were titered using a custom ordered AAV stock purchased from Virovek (Hayward, CA) as the reference standard. AAV titer quantification was performed using qPCR with the StepOne Plus Real Time PCR System (Applied Biosystems), FastStart Universal SYBR Green Master (Roche, Basel), and QPCR primers for an approximately 100 bp fragment of the woodchuck hepatitis virus post-transcriptional response element (WPRE) found in all our adeno-associated virus vectors. The titers for the five AAV stocks ranged between 1.37×10^{12} to 3.34×10^{13} viral genome (vg)/mL.

METHOD DETAILS

Immunohistochemistry

3 to 5 month-old *CACNG5-Cre* mice were transcardially perfused with 4% paraformaldehyde (PFA) in 0.1M sodium phosphate buffer (PBS). Brains were post-fixed overnight in 4% PFA and 50 μm thick vibratome sections were prepared. For detection of GAD67 sections were rinsed 3x10min in PBS and blocked in 3% normal donkey serum with 0.3% Triton-X in PBS for 2 hr, and incubated overnight with primary antibody (mouse α -GAD67, 1:500, Millipore MAB5406) in blocking buffer. Following 3x10min washes in PBS the sections were incubated with secondary antibody (Alexa Fluor 594-conjugated donkey α -mouse, 1:200, Invitrogen A21203) for 2 hr at room temperature. For simultaneous detection of Cre recombinase and PCP4 sections were incubated with both primary antibodies (mouse α -Cre, 1:1000, Millipore MAB 3120 and rabbit α -PCP4, 1:500, Santa Cruz sc-74816) in blocking buffer. Following 3x10min washes in PBS the sections were incubated with both secondary antibodies (Alexa Fluor 488-conjugated donkey α -mouse, 1:200, Invitrogen A21202 and Alexa Fluor 594-conjugated donkey α -rabbit, 1:200, Invitrogen A21207). Fluorescent images were collected (Leica DM6000B epifluorescent microscope 5x, 10x objective) of sections containing the dorsal hippocampus (AP -1.58 to -1.94 from bregma; Allen Brain Atlas).

In Vivo Electrophysiology

Subjects

All mice were male from the *Cacng5-Cre* line 181, hemizygous for the Cre transgene and aged between 3 to 5 months. All experimental protocols were approved by the RIKEN Institutional Animal Care and Use Committee.

Tetrode Drives

Custom microdrives were manufactured with the assistance of the Advanced Manufacturing Support Team, RIKEN Center for Advanced Photonics, Japan. The drives contain eight independently adjustable nichrome tetrodes (14 μm) (TT), gold-plated to an impedance of 200 to 250 k Ω , arranged in two rows of 4 TT, each of them running along the CA3 to CA1 axis of the dorsal hippocampus.

Injection of AAV into CA2 and Tetrode Drive Implantations

Mice were anesthetized using Avertin (2, 2, 2-tribromoethanol; Sigma-Aldrich, 476 mg/kg, i.p) and placed into a stereotactic frame (Kopf). AAV was microinjected bilaterally into CA2 (coordinates from bregma: AP -1.5 mm; ML ± 1.8 ; DV -1.5 ; 500nl/hemisphere; injection speed: 100nL/min; post injection waiting period: 10 min). Control mice (N = 9) were injected with AAV.DJ/8.DIO.EF1a.mCherry (3×10^8 vg) and CA2-TeTX mice were injected with either AAV.DJ/8.EF1a.DIO.TeTX.2A.mCherry (3×10^8 vg; N = 5) or AAV.DJ/8.CaMKII.DIO. TeTX.2A.mCherry (3×10^8 vg; N = 3). In CA2-DREADD experiments control mice (N = 6) were injected with AAV.DJ/8.DIO.EF1a.mCherry (9×10^8 vg) and CA2-DREADD mice were injected with AAV.DJ/8.hSyn.DIO.hM4D.Gi.mCherry (9×10^8 vg; N = 7). The recording drive was placed over the injection site in the right dorsal hippocampus with recording tetrodes extending approximately 1 mm.

Linear Probe

A 4-shank multi-site silicon probe (A4x16-3.6/3mm-50-430-177; NeuroNexus) mounted on an adjustable custom made microdrive (Advanced Manufacturing Support Team, RIKEN Center for Advanced Photonics) was implanted 1.5mm posterior of bregma, running laterally along the CA3 to CA1 axis of the right dorsal hippocampus at a depth of approximately 1.5 mm from the brain surface.

Experimental Protocol CA2-TeTX Mice

2 days post-surgery, TTs or linear probe (5th site from top of the second shank) were lowered over several days to *stratum pyramidale* (SP) while mouse rested in a small bucket (sleep/rest box 15cm diameter). Recordings commenced once SP was reached based on the presence of SWRs and high amplitude spiking. At the start of each day the TTs were finely adjusted to maximize cell yield. Daily recordings on the linear track (LT1: 140x10 cm, semi-transparent gray 15cm walls) were bracketed by rest/sleep sessions (~ 30 min) in a small familiar sleep box. Following onset of theta-associated pathophysiology two additional linear tracks were also added to the experimental protocol (LT2: 140x10 cm white and black striped 15cm wall, bubble wrap flooring and banana odor; LT3: 140x10cm brown 15cm walls, electric tape flooring and almond odor), as well as two open fields (High-walled square box 40 \times 45 cm bubble wrap flooring; High-walled round box 40 cm diameter and acetic acid odor).

Experimental Protocol CA2-DREADD Mice

2 days post-surgery, TTs were lowered over several days to SP while mouse rested in a small bucket (sleep/rest box 15cm diameter). Recordings commenced from two weeks post-injection. At the start of each day the TTs were finely adjusted to maximize cell yield. The recordings consisted of a rest/sleep session (~ 30 min in small bucket) followed by a run on a familiar track (LT1). Mice then received an intraperitoneal injection of 2mg/kg clozapine-N-oxide and changes of the CA2 spiking were monitored over a 45 min

recording session. Inhibitory action of the G_i DREADD was observed to reach full efficacy about 20 min post-injection. Following CA2 shutdown all mice were exposed a second time to LT1 followed by a final rest/sleep session.

After recordings were completed mice underwent terminal anesthesia with Avertin and electrode positions were marked by electrolytic lesioning of brain tissue (30 μ A current for 5 s through each tetrode). After transcardial perfusion with 4% paraformaldehyde (PFA) brains were removed and post-fixed for another 24 hr in 4% PFA. Coronal slices (50 μ m thick) were prepared on a Vibratome (Leica) and inspected by standard light microscopy to confirm electrode placement. Hippocampal subregions were defined according to standard criteria (Boccaro et al., 2015; Lorente de No, 1934), using the expression of the mCherry marker in CA2 PCs as a reference. For tetrodes in CA3 we defined CA3a, CA3b and CA3c as the distal 33% (closest to CA2), middle 33% and proximal 33% (closest to DG) respectively.

In Vitro Electrophysiology

Stereotaxic Injection

The adeno-associated viruses AAV.EF1a.DIO.TeTX.2A.mCherry, AAV.EF1a.DIO.mCherry, and AAV.EF1a.DIO.hChR2(H134R).EYFP were used at 3×10^8 vg. 500 nL of virus was injected bilaterally into the hippocampus of 6–8 week-old *Cacng5-Cre* mice at 100 nL/min and the injection cannula were removed 5 min after infusion was complete. Injections were centered on: AP: –1.5 mm (relative to bregma); ML: 1.8 mm (relative to midline); at a depth of 1.5 mm from the brain surface. The resulting infected area spanned at least 2 mm along the longitudinal axis of the hippocampus.

Slice Preparation

400 μ m transverse hippocampal slices were prepared between 8 and 15 days following viral injection for the TeTX experiments. For ChR2 alone, slices were prepared between 2 – 6 weeks post-injection. Animals were euthanized in accordance with institutional regulations under isoflurane anesthesia. Animals were intracardially perfused with oxygenated cutting solution containing (in mM): 93 NMDG, 2.5 KCl, 1.25 NaH₂PO₄, 30 NaHCO₃, 20 HEPES, 25 Glucose, 2 thiourea, 5 Na-Ascorbate, 3 Na-pyruvate, 0.5 CaCl₂, 10 MgCl₂, 93 HCl. Hippocampi were removed and placed upright into an agar mold and cut with a vibratome (Leica VT1200S) in ice-cold solution and transferred to 30°C ACSF (in mM: 125 NaCl, 2.5 KCl, 10 glucose, 26 NaHCO₃, 1.25 NaH₂PO₄, 2 Na Pyruvate, 2 CaCl₂ and 1 MgCl₂) for 30 min and maintained at room temperature for at least 1.5 hr prior to recording. All experiments were performed at 33°C. Cutting and recording solutions were both saturated with 95% O₂ and 5% CO₂ (pH 7.4).

Electrophysiological Recordings and Analysis

Whole-cell recordings were obtained from hippocampal PCs in current clamp mode held at –73 mV with a patch pipette (3–5 M Ω) containing (in mM): 135 KMethylSulfate, 5 KCl, 0.1 EGTA-Na, 10 HEPES, 2 NaCl, 5 ATP, 0.4 GTP, 10 phosphocreatine and 5 μ M biocytin (pH 7.2; 280–290 mOsm). Inhibitory currents were recorded with pipette solution containing 135 CsMethylSulfate instead of KMethylSulfate. When necessary, GABA_A and GABA_B currents were blocked with 1 μ M SR95531 and 2 μ M CGP55845, respectively (Tocris). The liquid junction potential was ~2 mV and membrane potentials were corrected to account for this. Series resistance (typically 12–18 M Ω) was monitored throughout each experiment; cells with more than 15% change in series resistance were excluded from analysis.

Photostimulation with 0.1 ms pulses of blue light was achieved using a 473 nm light-emitting diode (controlled by a CoolLED model PE-100) driven by a TTL pulse. The light intensity used was between 10–50 mW/mm². This was measured at the appropriate focal length under the objective with a Fieldmate model light meter (Coherent) at different power intensities. To examine DG-CA3 synaptic transmission, synaptic potentials were evoked by mono-polar stimulation with a patch pipette filled with ACSF and positioned centrally in the granule cell layer nearly at the border of the polymorphic layer. For extracellular recordings examining CA3-CA1 fEPSP and CA3-CA3 fEPSP, recording electrodes filled with 1 M NaCl were placed in SR of CA1 and CA3b respectively. For CA3-CA3 measurements, a monopolar stimulating electrodes filled with ACSF were placed in the SR of CA2 200 μ m away in CA3a/b and for CA3-CA1 measurements, the stimulation electrode was placed 200 μ m toward the subiculum in CA1 SR. The stimulating pipettes were frequently moved to optimize evoked responses. GABA receptor blockers 1 μ M SR95531 and 2 μ M CGP55845 were bath-applied following dilution into the external solution from concentrated stock solutions. We used pClamp10 and Axograph X software for data acquisition.

Recorded cells were filled with biocytin and post hoc labeling of filled cells with streptavidin-Alexa-647 was performed along with immunohistology to confirm consistent level of expression of limited to CA2 PCs. ChR2 was labeled with chicken α -GFP (Life Technologies) diluted 1:10000, mCherry with rat α -dsRed (Life Technologies) diluted 1:2000 and Alexa 488 conjugated goat α -chicken diluted 1:500 and Cy3-goat α -rat. Slices were mounted with ProLong Gold (Thermofisher) and images were taken with a Zeiss 710LSM confocal microscope. Image analysis was performed with ImageJ.

Mouse Behavior

Contextual Fear Conditioning

All experiments were conducted two weeks after the infusion of AAV.EF1a.DIO.TeTX.2A.mCherry or AAV.EF1a.DIO.mCherry bilaterally into CA2 of 3–5 month male *Cacng5-cre* mice hemizygous for the transgene, in a manner identical to the one used for recording experiments. CA2-TeTX (N = 8) and mCherry control (N = 8) mice were trained in contextual fear conditioning. Shocking and testing were conducted in dedicated behavioral training rooms located in the animal facility during the light cycle. All experiments were conducted and analyzed by scientists blind to the virus injected (TeTX versus mCherry (control)). On the day of training the mice were

brought into a room lit with overhead fluorescent lighting and containing four conditioning chambers. The chambers had plexiglass fronts and backs and aluminum side walls, and measured 30 × 25 × 21 cm (Med Associates ENV-008; Georgia, VT). The chamber floors consisted of 36, 3.2 mm diameter stainless steel rods spaced 7.9mm apart connected via a cable harness to a shock generator. The chambers were cleaned between mice with 70% ethanol and a solution of 1% acetic acid was placed beneath the chambers during the experiment to provide an olfactory cue. All experiments were conducted using FreezeFrame software. Mice were placed in the chamber and allowed to freely explore for 3 min at which time they received a single unsignaled foot shock (2," 0.75mA). 1 min later animals were returned to their home cages. The next day the mice were returned to the identical context and freezing was monitored for 5 min. During all sessions, the animal's activity in the chamber was recorded using FreezeFrame software (Actimetrics; Wilmette, IL). Freezing behavior was assessed from the video image of the mouse with a minimum bout time of 2 s.

Context Habituation

All experiments were conducted two weeks after the infusion of AAV.EF1a.DIO.TeTX.2A.mCherry or AAV.EF1a.DIO.mCherry bilaterally into CA2 of 3-5 month male *Cacng5-cre* mice hemizygous for the transgene, in a manner identical to the one used for recording experiments. Two weeks after the viral-infusion CA2-TeTX (N = 8) and mCherry control (N = 8) mice were first habituated to handling and transport. All mice were allowed to explore Box A for 5 min daily over 2 days by an experimenter blind to genotype. Box A is a round arena, 40 cm in diameter, with 45-cm-high white walls, a green textured floor, 0.1% isoamyl alcohol (banana) scent, and contains two small metallic objects in fixed locations. Box B is a square arena (40 cm sides) with blue walls, a green and brown textured floor lined with bubble wrap, 0.1% benzaldehyde (almond) scent, and two fixed plastic objects, distinct from those in Box A. On Day 3 the mice were allowed to explore Box A for 5 min, were returned to their home cage for 1 hr, and then placed in the new Box B for 5 min. The animal's position was tracked with an overhead camera connected to a computer running ANY-maze software (Stoelting). Analysis of the distance traveled for each animal was conducted using ANY-maze and averaged across each genotype and context.

KA Seizure Induction

All experiments were conducted two weeks after the infusion of AAV.EF1a.DIO.TeTX.2A.mCherry or AAV.EF1a.DIO.mCherry bilaterally into CA2 of 3-5 month male *Cacng5-cre* mice hemizygous for the transgene, in a manner identical to the one used for recording experiments. Two weeks after the viral-infusion CA2-TeTX (N = 17) and mCherry control (N = 15) received an intraperitoneal injection of kainic acid (Sigma K0250; 30mg/kg in saline) and placed into a clean cage. Animals were continuously monitored for 120 min following injection and seizure behavior was scored according to a modified Racine scale by an experimenter blind to the genotype (Racine, 1972): stage 0-normal behavior, stage 1-immobility and rigidity, stage 2-head bobbing, stage 3-forelimb clonus and rearing, stage 4- continuous rearing and falling, stage 5- clonic-tonic seizure, stage 6- death). The maximum Racine score was recorded every 10 min and the cumulative seizure score was calculated by summing these scores across all 12 bins of the 120 min experiment.

QUANTIFICATION AND STATISTICAL ANALYSIS

In Vivo Electrophysiology

Data Processing and Unit Isolation

Data files from each dataset were split by manually recorded trial timestamps using EventSessionSplitter software (Neuralynx). Artifacts in the animal's positional values caused by the obscuring of diodes were removed using a custom written algorithm and the positional data were smoothed with a Gaussian kernel of 0.05 standard deviation (SD) width. Single units were isolated manually, in SpikeSort3D software (Neuralynx), by drawing cluster boundaries around the 3D projection of the spike features. Unfortunately the magnitude of the increase in the LFP power during the actual place-specific hyperexcitability episodes, along with the strong concurrent high-frequency oscillation, often led to saturation of the signal and prevented isolation of single unit activity during these periods, thus they were removed from the analyses. The boundaries were tracked across same-day recording trials (Sleep/LT/Sleep etc.) to ensure cluster stability. Clusters that had greater than 0.5% of their spikes violate a minimum 2 ms inter-spike interval (ISI), fire less than 50 spikes or display an isolation distance measure (Schmitzer-Torbert et al., 2005) < 10 were excluded from further analyses. Remaining units were classified as pyramidal cells if their average spike width was > 200 μ S and had a complex spike index \geq 5, (CSI; McHugh et al., 1996). Animal velocity was calculated based on recorded position values and corresponding timestamps and then smoothed with a 2.5 SD. Gaussian kernel. All subsequent analyses were performed in MATLAB (MathWorks), using custom written scripts.

Single-Unit Properties

Firing rate maps were calculated by dividing the number of spikes falling into each 1cm x 1cm spatial bin by the total occupancy time of that bin and were subsequently smoothed with a 1 SD. Gaussian kernel; unvisited bins were excluded. Peak firing rate was defined as the rate in the spatial bin containing the maximal firing rate value within each rate map. Mean firing rate was calculated by dividing the number of spikes occurring in where velocity exceeded 2 cm/s by that period's duration and followed by averaging these values. A place field was defined as a set of contiguous spatial bins surrounding the bin where the maximal firing rate was observed. Place cells were required to have a minimum field size equivalent to 6 bins (1cm x 1cm bin size), a mean firing rate > 0.2Hz, a peak firing rate > 1.0Hz and a positive signal to noise ratio. Place field size was defined as the number of spatial bins where place cell field firing exceeded 20% of the peak firing rate.

Complex spike index (McHugh et al., 1996). CSI is defined as $CSI = 100 * (\text{pos} - \text{neg})$, where "pos" is the number of inter-spike intervals positively contributing to the CSI, i.e., preceding spikes with larger amplitudes and following spikes with smaller amplitudes

(complex bursts) occurring within 3 ms (refractory period) and 15 ms (maximum inter-spike interval defining a burst); “neg” is the number of inter-spike intervals that contribute negatively to CSI, i.e., violating either or both these rules.

Spatial Information (bits per spike) was calculated as previously reported in (Skaggs et al., 1993); briefly $SI = \sum (P_{\text{spk}(i)} * \log_2 (P_{\text{spk}(i)} / P_{\text{occ}(i)}))$, where $P_{\text{spk}(i)}$ is the probability of spiking in bin “i” and $P_{\text{occ}(i)}$ is the occupancy probability in bin “i.” P_{spk} and P_{occ} are computed from the rate and occupancy maps respectively.

CNO-Mediated Inhibition

(Figure 5B) To quantify the effect of CNO administration we calculated the mean firing rate for each pyramidal cell during the rest period before the first track run of the day (sleep1), 15 min prior to CNO injection, and the mean firing rate during the rest session following the last track run of the day (sleep3), 50 min after CNO injection. The normalized change in mean rate was calculated by the following formula: $(FR_{\text{sleep3}} - FR_{\text{sleep1}}) / (FR_{\text{sleep1}} + FR_{\text{sleep3}})$. A value of -1 represents a complete shutdown of spiking following CNO injection. Values were averaged across hippocampal subregion and group.

Analysis of Spatial Correlation Firing in the CA2-DREADD Mice

Due to the pronounced directionality of place cell firing during the linear track behavior task, this analysis was performed on a directional lap-per-lap basis. First, a “lap” – the time period when the mouse is running along the central part of the track (i.e., excluding time spent in the extremity of the box) was detected using a custom iterative algorithm. For each trial, the quality of the lap detection was confirmed visually by plotting the laps on top of the mouse’s trajectory. Then a 1D version of the firing rate map – i.e., “firing rate curve” was calculated for each pyramidal cell based on the lap’s timestamps. In order to exclude place cells whose place fields were located too close to the ends of the track we limited the set of cells based on a “Peak2EoT_proxy” measure. The measure was calculated based on a 2D firing rate maps and correspond to the proximity of the place field to the end of the track, reaching value 0.5 if place field peak was located in the middle of the track and 0 for place fields at either end. The threshold was set to 0.1. The spatial correlation firing was assessed by calculating Pearson’s correlation coefficient between the firing rate curves of the same cells before and after CNO injection.

Unit Activity Prior to Onset of Place-Triggered Hyperexcitability

(Figure 4B) To identify place triggered hyperexcitability events the continuous wavelet transform (CWT) was then applied to the unfiltered LFP using complex Morlet wavelets returning amplitudes at 350 intervals between 300-1000 Hz. The mean amplitude across all frequencies was calculated, z-scored and smoothed with a 500 ms Gaussian kernel. Epochs exceeding 2SD above the mean were identified as putative events, epochs occurring within 500ms of each other were concatenated into one event. Of these periods only those lasting > 1.5 s with a mean velocity > 6 cm/s were considered as place triggered hyperexcitability events. The spike rates of all CA3 and CA1 pyramidal cells were calculated in 250 ms bins for the preceding 5 s, lined up to the start times of these events, with periods of immobility (< 2 cm/s) excluded. Since control mice did not show comparable changes in LFP amplitude, laps were identified where velocity was consistently > 6 cm/s for periods greater than 5 s. We aligned the ends of these periods (where velocity < 2 cm/s) and calculated spike rates (as for CA2-TeTX mice) for the preceding 5 s. Percentages of co-active cells were defined as the fraction of cells firing 1 or more spikes in a given 250 ms temporal bin.

Analysis of Multiunit Spiking and Place-Field Shift in the CA2-DREADD Mice

(Figure 5C–5E) Place cell rate maps were constructed for all CA3 and CA1 place cells post-CNO individually for each mouse, comprising only spikes when animal velocity > 6 cm/s. Rate maps were subsequently z-scored and a population mean calculated per mouse. Individual animal rate maps were circularly shifted to align their respective maxima across subjects. The same cells were identified in the pre-CNO condition and for cells which exhibited a spatial shift in their peak firing bin following CNO of > 10 cm, the magnitude of the shift in cm, the direction of shift (toward or away from the aligned population maxima) and change in z-scored firing rate were calculated. The relationship between place field shift and change in z-scored firing rates were quantified with the Pearson’s correlation coefficient, separately for controls and DREADD expressing animals.

Local Field Potential Analysis

The raw local field potential (LFP) data were downsampled using custom software written in C to 1627.8 Hz (a factor of 20), followed by quality control measures which excluded any signals that were either saturated or had a signal (4-12 Hz) to noise (45-55 Hz) ratio > 6 dB. A low-pass filter with a cut-off frequency equal to half the target sampling frequency was applied to the LFP prior to downsampling to prevent signal distortion.

Spatially Triggered Network Hyperexcitability Event Detection

Events (Figures 3B–3D, S4, and S5) were detected for each subject using a single CA1 LFP channel displaying maximum power in theta band (4-12 Hz) among other LFP channels in that recording session. LFPs were downsampled to 203.5 Hz and filtered in the theta band using the `eegfilt` function (EEGLAB; Delorme and Makeig, 2004). Instantaneous theta magnitude was calculated as an absolute value of Hilbert transform, which was subsequently smoothed with 0.5 s Gaussian kernel. Finally, Spatially triggered network hyperexcitability events were defined as periods where the magnitude of theta exceeded a 3SD threshold above the mean for at least 0.2 s.

Epileptiform-like Discharges

(EDs) were detected using the instantaneous magnitude (absolute value of Hilbert transform) of the LFP filtered between 1-100 Hz and smoothed with 10 ms Gaussian window. Candidate ED events were identified as times when magnitude exceeded 6SD above mean for at least 20 ms. Visual quality control of the EDs detection revealed its sensitivity to non-ED related low frequency deflections of the LFP. To avoid such contamination we detected the deflections using the same method as for EDs, using the following

parameters (203.5 Hz sampling frequency, 1–12 Hz band pass filter, 0.5 s Gaussian window, 3SD magnitude threshold, 0.2 s duration threshold) and excluded temporally overlapping events. Inter-region lag/lead delays for EDs were derived from the absolute maximum value of the wide band LFP signal.

Ripple Detection

Ripple events were detected using modifications to methods described previously (Csicsvari et al., 1999). Since EDs typically displayed a much higher intrinsic frequency than ripples, wide band LFP were band-pass filtered between 80 and 500 Hz using 69 orders Kaiser-window FIR zero-phase shift filter. The absolute value of Hilbert transform was then smoothed with 50 ms Gaussian window and candidate ripple events were detected as periods where magnitude exceeded 3SD above the mean for > 30 ms. Of the events, the initiation and termination periods were defined as periods when the magnitude returned to the mean. Multi-unit activity (MUA) recorded from the same tetrode as the LFP was converted to instantaneous firing rate and smoothed, to allow detection of firing bursts using the same thresholds as described for LFP. Candidate ripple events not coincident with MUA bursts were excluded from subsequent analysis. For cleaner detection of ripple frequency for each ripple, a multitaper method was performed on the product of each filtered ripple waveform and a Hanning window of the same length. Peak amplitude of the ripple-associated sharp waves was defined as a maximal value of amplitude of band-pass filtered (1–20 Hz, Butterworth filter, order 3) LFP.

Current Source Density Analysis

One-dimensional current source density (CSD) maps (Figure 6D) were calculated across depth as the second spatial derivative of the extracellular local field potential recordings. Sharp-wave ripple events for this analysis were detected by first band-pass filtering LFPs between 90–250 Hz using a Hamming-window based FIR filter and calculating the root-mean square power, during sleep sessions. Ripple candidate events were classified as events exceeding 5SDs above the mean and terminated when values fell below 1.5SDs. For our purposes candidate events were only considered ripples if they had duration between 30 and 300 ms and animal velocity remained at 0 cm/s throughout. Ripple CSD maps were generated by averaging over successive events centered on the peak ripple power. ED CSDs were calculated as those for ripples with the exception that the band-pass filter used for detection was widened (90–400 Hz), owing to their greater mean frequency.

Wavelet Analysis of Spatially Triggered Network Hyperexcitability Events and EDs

LFPs with sampling frequencies of either 813.9 Hz (for spatially triggered network hyperexcitability events) or 1627.8 Hz (for EDs) were convolved with a Morlet family wavelet (with parameter 7; spacing between discrete scales 0.01). For Figure 2F bottom, middle and Figure 3B LFP were prewhitened (3–400 Hz, 20–500 Hz, and 30–500 Hz respectively) prior to computation of wavelet transform to damp lower frequencies. For quantification of HFO occurred on the rising phase of theta wave (Figure 2G) the instantaneous phase of theta-band pass filtered signals (4–12 Hz) was calculated using the Hilbert transform. The continuous wavelet transform (CWT) was then applied to the unfiltered LFP using complex Morlet wavelets returning amplitudes at 186 intervals between 30–400 Hz. Phase time-series were binned and the mean wavelet amplitude calculated by phase. The MATLAB script for wavelet analysis was provided by C. Torrence and G. Compo (Torrence and Compo, 1998), available at <http://paos.colorado.edu/research/wavelets/>

Power Spectrum Density

(Figure 2A) Periods where animal velocity fell below 6 cm/s were excluded. Power spectra for all control laps and mutant laps without hyperexcitability events were calculated using the pwelch function in MATLAB, using 0.63 s data segments with a 50% overlap. Power was defined as the area from the resultant spectra, in the following bands: theta (4–12 Hz), gamma (30–80 Hz), HFO (200–400 Hz). Hyperexcitability periods in the CA2–TeTX mice were first segregated and treated separately. This was performed by manually setting upper and lower amplitude thresholds for each subject, data within these bounds were classified as non-event periods, whereas data exceeding these values were taken with a 1-s surrounding window and treated as event periods.

Per-Lap PSD Calculation, Theta-Power-Based Directionality Index, and Spatial Information

In order to numerically quantify directional asymmetry of spatially triggered network hyperexcitability events we calculated PSD separately for left and right laps (excluding boxes at track ends) by using pwelch function with 2048 samples windows size (1.26 s), 50% overlap and 4096 FFT points (2.52 s). PSD curves corresponding to the signal saturation and time periods when animal's velocity fell below 6 cm/s were excluded. The resulting subset was averaged across time, yielding single PSD curve for each lap. "Directionality Index" was defined as $DI = \frac{\text{abs}(\text{PSD}_L - \text{PSD}_R)}{(\text{PSD}_L + \text{PSD}_R)}$, where PSD_L is an average PSD value in theta (4–12 Hz) band for all "left laps"; PSD_R is an average PSD value in theta band for all "right laps." Spatial Information is a measure typically used for characterization of place cells activity (Skaggs et al., 1993) based on firing rate/occupancy curves. Here we hypothesized a similarity between theta-associated pathophysiological events and place cells activity and therefore we calculated LFP-derived spatial information based on instantaneous theta magnitude along each lap and occupancy time of each spatial bin of the track.

Velocity and Traveled Distance

These data were calculated from animal's position on a per-video frame basis (30 Hz sampling frequency and 0.26 cm/pixel spatial resolution), with acceleration and deceleration (Figure S3) defined as positive and negative difference between adjacent velocity values respectively. The strength of correlation between animal's velocity and theta power was calculated as the distribution of z-scored instantaneous theta power values across 32 logarithmically spaced velocity bins (1–32 cm/s), excluding signal saturations and periods when theta-associated pathophysiological events occurred. Instantaneous velocity values were up sampled from 30 Hz to the sampling frequency of LFP traces using linear interpolation. Coefficient of variation (CV) of theta power across velocity was defined as ratio of standard deviation of the power values correspondent to velocity values within each velocity bin to the mean

velocity value for the same bin. CV of theta power across space was defined as ratio of standard deviation of the power values correspondent to animal's longitudinal coordinate on a track within each spatial bin to the mean longitudinal coordinate value within the same spatial bin.

Theta Modulation of Pyramidal Cells

(Figures 4C and S5) The phase relationship between spikes and theta LFP was calculated as previously described (Siapas et al., 2005). Briefly, LFP traces were band-pass filtered in the theta band. Instantaneous theta phase was derived from the Hilbert-transformed theta filtered signal. Peaks and troughs were assigned 0 and 180 degree phases respectively, with spike phase calculated using interpolation, a method not sensitive to theta asymmetry. The resultant phases were converted to firing probability histograms (10 degree bin size), only when velocity exceeded 6 cm/s. Significance of the phase locking, preferred firing phase, strength of modulation, mean resultant length (MRL) values and statistical comparison of phase values were calculated using functions from Circular Statistics Toolbox (Berens, 2009).

STATISTICS

Analyses were performed using custom written scripts in MATLAB (The MathWorks, Inc), Origin Pro (Origin Lab) or in Prism 5 (GraphPad Software). Data were first tested for normality with the Kolmogorov-Smirnov test and/or the D'Agostino and Pearson omnibus normality test prior to further statistical analysis to determine whether parametric or non-parametric statistical tests were suitable. For pairwise comparisons Student's t test or Mann Whitney tests were used as noted, for multiple group comparisons we employed Kruskal-Wallis test or one or two-way ANOVAs with repeated-measure (RM) where appropriate, followed by Dunn's or Tukey's tests for multiple comparisons. All circular statistics were performed using the MATLAB Circular Statistics Toolbox. No statistical methods were used to pre-determine sample sizes, instead we opted to use group sizes of similar previously published studies (McHugh et al., 2007; Nakashiba et al., 2008) to ensure variance was kept to a minimum between genotypes and cell quantities. Unless noted, all plots with error bars are reported as mean \pm SEM and all samples are reported as number of mice (N) and number of cells (n).

DATA AND SOFTWARE AVAILABILITY

Custom MATLAB scripts developed for the analyses of the in vivo electrophysiological data are described in detail above. All custom scripts and data contained in this manuscript are available upon request from the corresponding author, Thomas McHugh (tjmchugh@brain.riken.jp).

Neuron, Volume 94

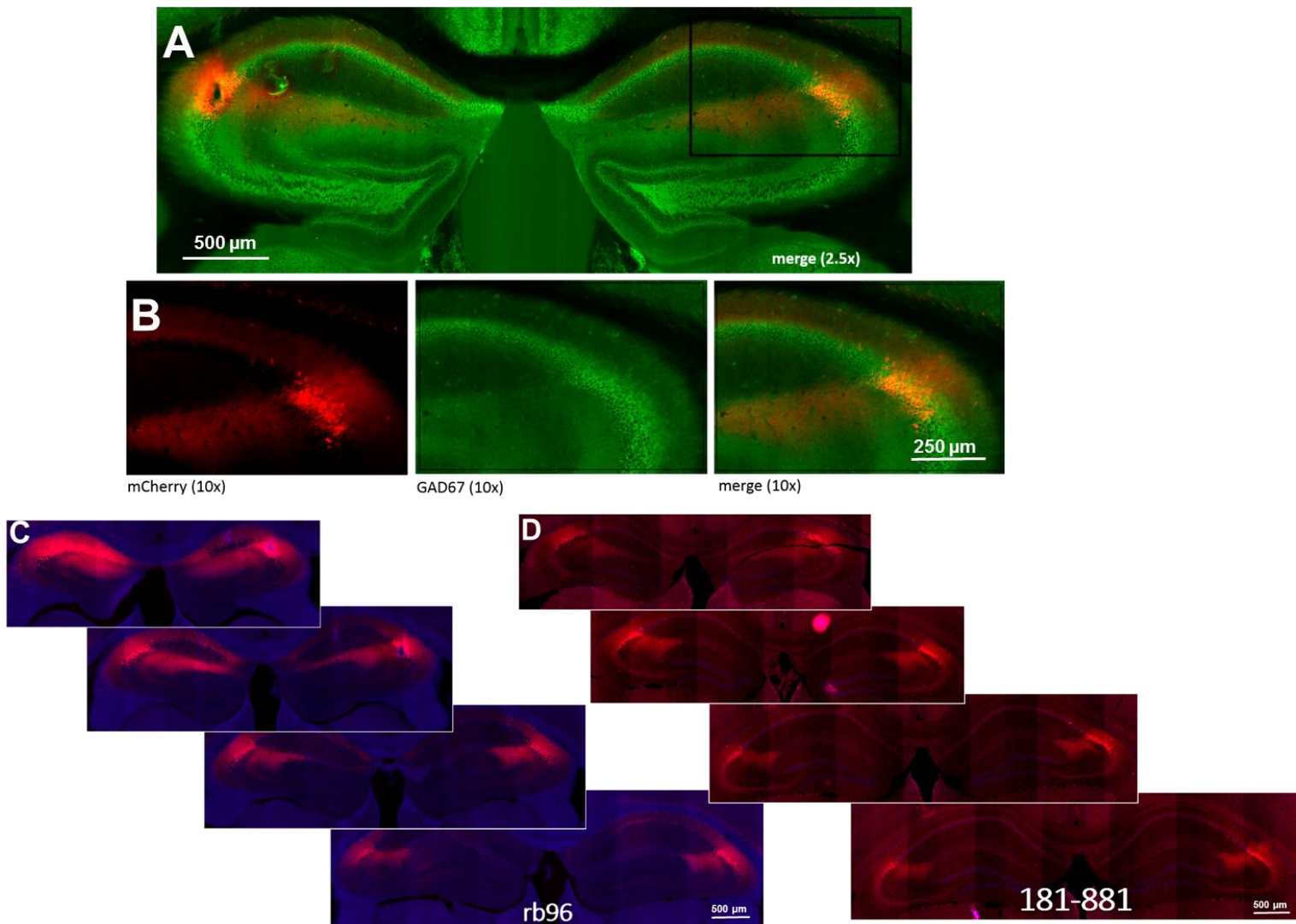
Supplemental Information

Chronic Loss of CA2 Transmission

Leads to Hippocampal Hyperexcitability

Roman Boehringer, Denis Polygalov, Arthur J.Y. Huang, Steven J. Middleton, Vincent Robert, Marie E. Wintzer, Rebecca A. Piskorowski, Vivien Chevalere, and Thomas J. McHugh

Figure S1. Cre-mediated Viral Expression is Confined to Pyramidal Cells in CA2 in the *Cacng5-Cre* Transgenic Line, Related to Figure 1



(A). Low magnification image of the dorsal hippocampus of a CA2-Cre mouse expressing virally-delivered mCherry. Red signal is unamplified mCherry fluorescence, green signal is α GAD67 antibody. Tetrode lesions are evident in the CA2 and CA1 in the left hippocampus.

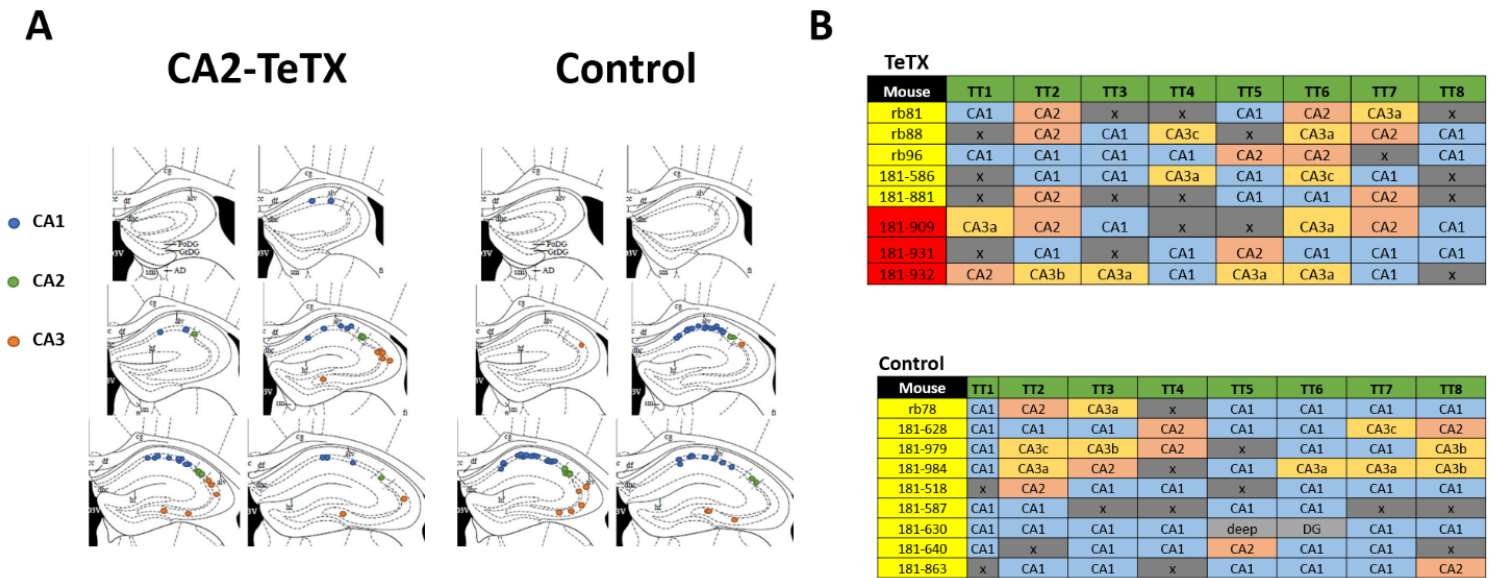
(B) 10x magnification of right hippocampus, as indicated by black box.

(C-D) Sections covering the dorsal hippocampus, from -1.0 mm to -2.5mm relative to bregma. *Cacng5-Cre* mice were bilaterally injected with Cre-dependent AAV.

(C) Mouse rb96 injected bilaterally with pAAV.EF1a.DIO.TeTX.2A.mCherry. Images were acquired with a Keyence BZ-X700 fluorescent microscope with a 20x objective and multiple field-of-views were registered and stitched using Keyence software to produce the final wide-field images.

(D) Mouse 181-81 injected bilaterally with pAAV.CaMKII.DIO.TeTX.2A.mCherry. Images were acquired with a Hamamatsu NanoZoomer Digital Pathology RS slide scanner using a 20x objective and multiple field-of-views were stitched using the Hamamatsu software to produce the final wide-field images.

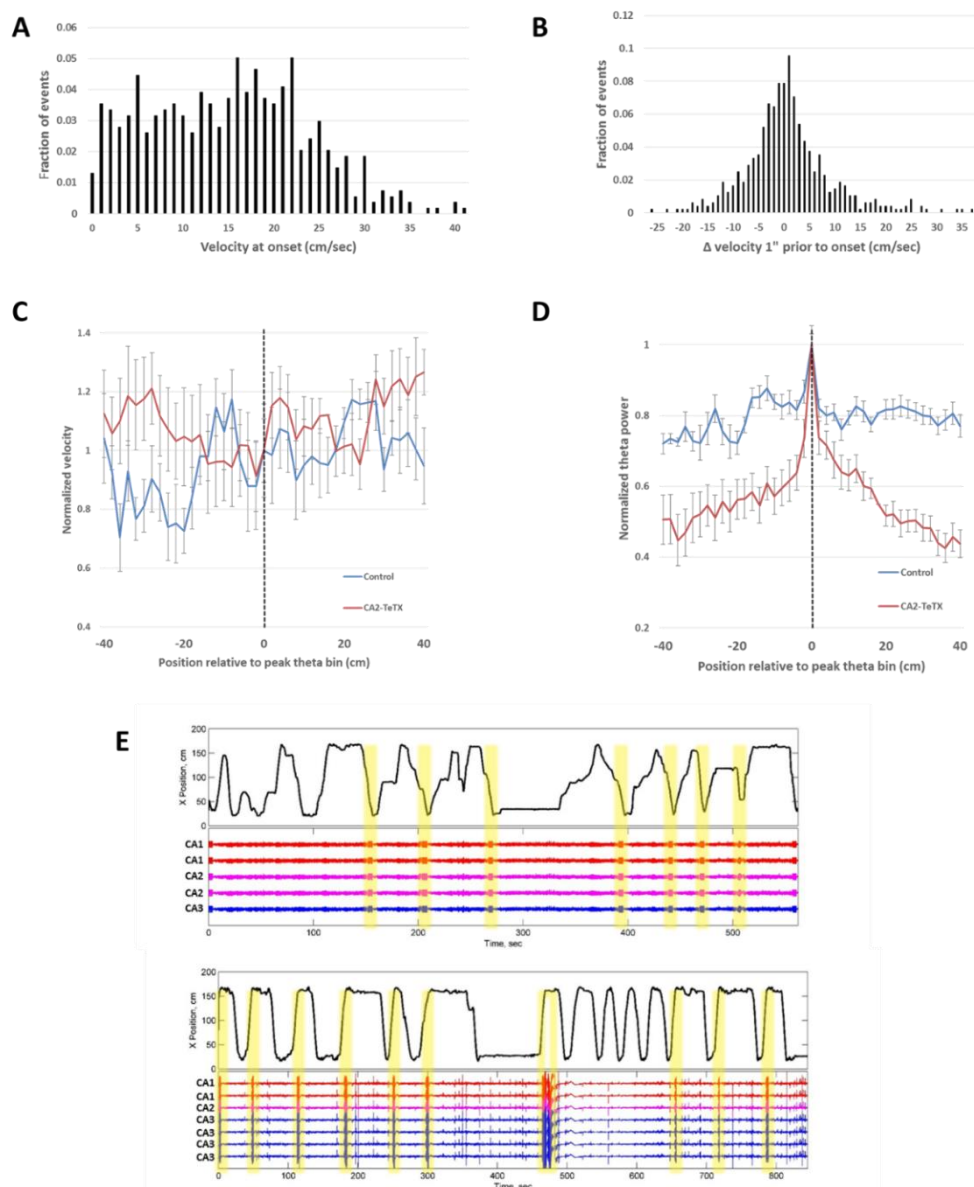
Figure S2. Recording Locations in CA2-TeTX and Control Mice, related to Figures 3, 4 and 6.



(A) Tetrode locations based on location of post-recording lesions in all CA2-TeTX (left) and all Control (right) mice. CA1: Blue, CA2: Green, CA3: Orange.

(B) List of all mice used in experiments and corresponding location of each tetrode (TT1 thru TT8). All Control and CA2-TeTX mice listed in yellow were injected with AAV containing the EF1 promoter. CA2-TeTX mice in red were injected with AAV containing the α CamKII promoter.

Figure S3. Hyperexcitability events are related to spatial position, not velocity, related to Figure 3



(A) Distribution of velocity of CA2-TeTX mice at the onset of spatially-triggered hyperexcitability events reveals no relationship between onset and a specific speed.

(B) Histogram of the change in velocity (acceleration/deceleration) in the one second prior to theta magnitude increase is distributed normally around zero.

(C,D) The spatial bin (2cm bin size) with the maximum average theta power was detected for each linear track session. All data plotted as mean±SEM

(C) Normalized velocity around the location of the spatial bin with the peak theta power demonstrates no clear relationship between velocity and relative position in either Control (blue) or CA2-TeTX mice (red).

(D) However when the peak bins from each session were aligned for each group and normalized theta was plotted by relative location to the peak, the spatial nature of the theta power increase was evident in the CA2-TeTX mice (red), but not Control mice (blue).

(E) Spatially triggered hyperexcitability occurs in all three CA fields. Wide-band LFP recordings (CA1: red, CA2: magenta, CA3: blue) and animals position (black trace, x-position) across time during one linear track session. Yellow boxes highlight large LFP events which occur at fixed track locations. Upper: mouse rb81, Lower: mouse 181-932

FIGURE S4. Example of Spatially-Triggered Hyperexcitability Events From All CA2-TetX Mice, Related to Figure 3.

Spatially-triggered hyperexcitability events are detected by increases in theta magnitude ($3\text{ SD} > \text{mean}$) and color coded by order of occurrence within each session from blue (first) to red (last). For track sessions the arrow indicates direction of the mouse, DI score indicates the directional bias of the events based on theta power and SI indicates the spatial information score calculated based on theta magnitude. Text in the upper left corner of each box indicates mouse ID and recording day, with virus injected at day zero.

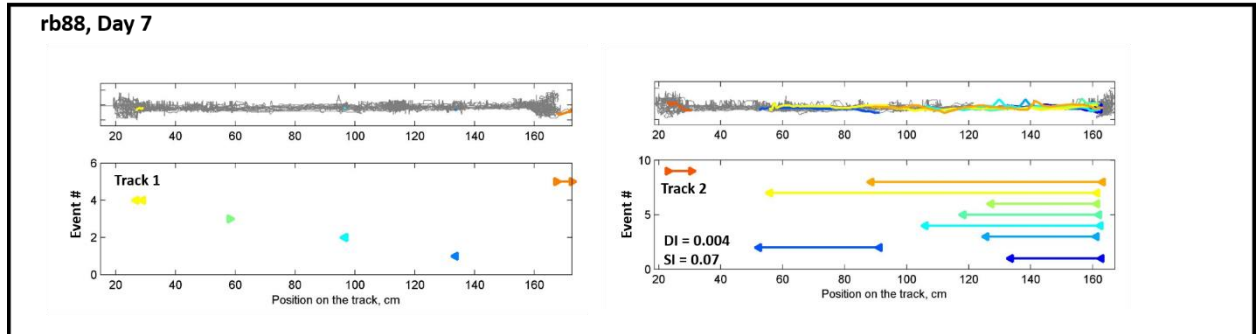
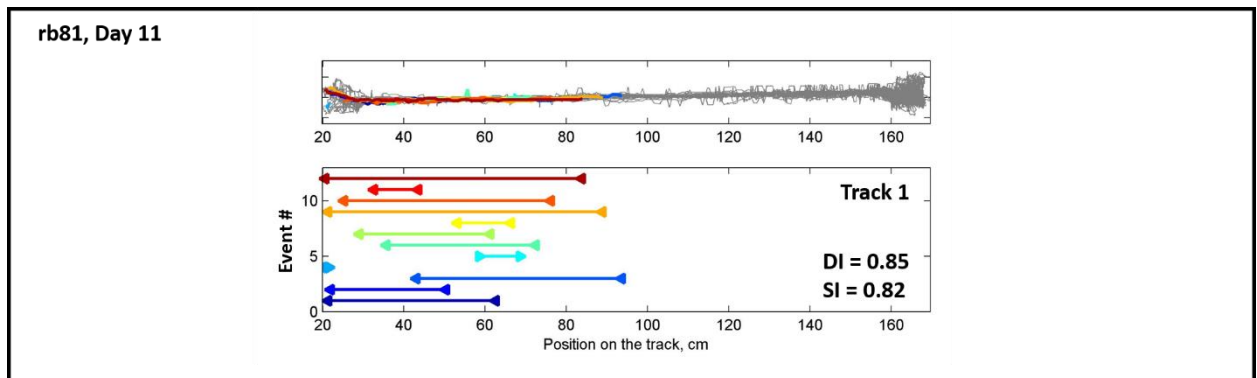


Figure S4 (cont.)

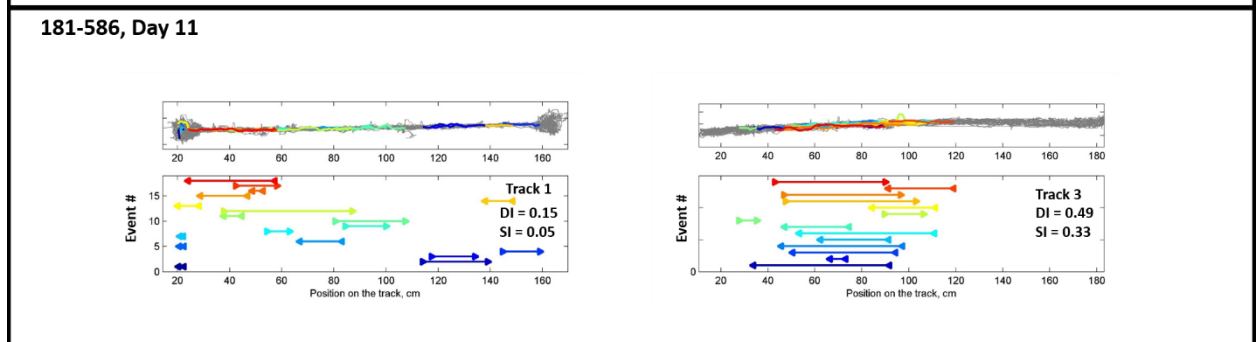
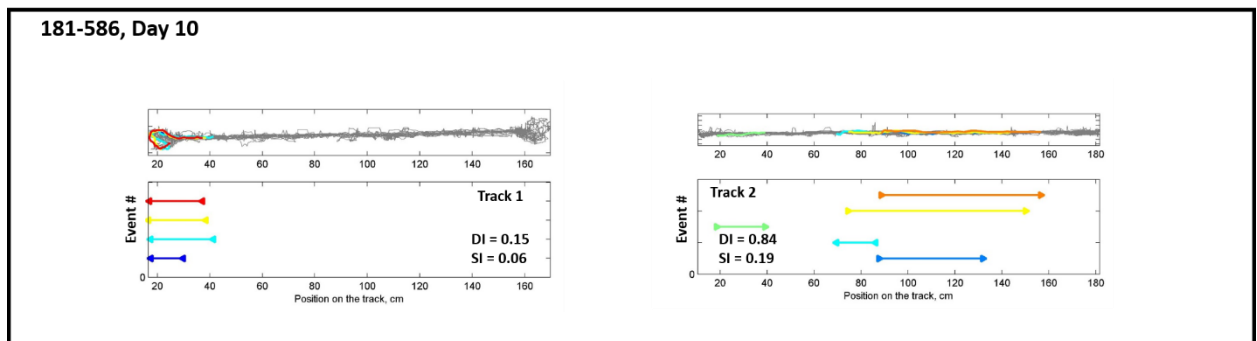
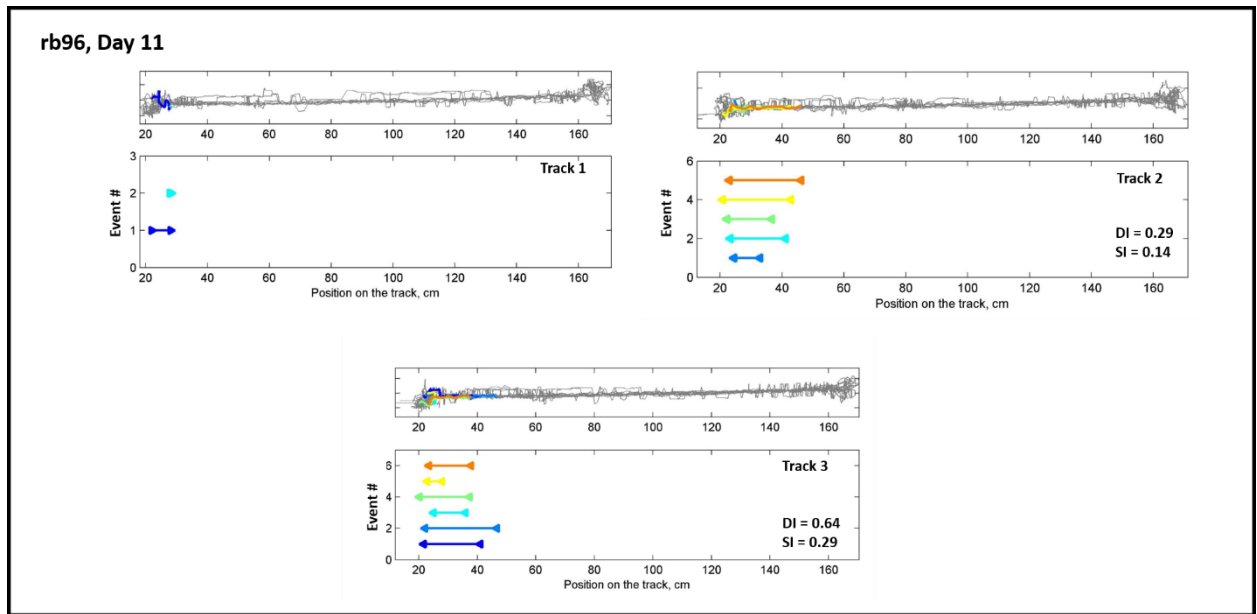


Figure S4 (cont.)

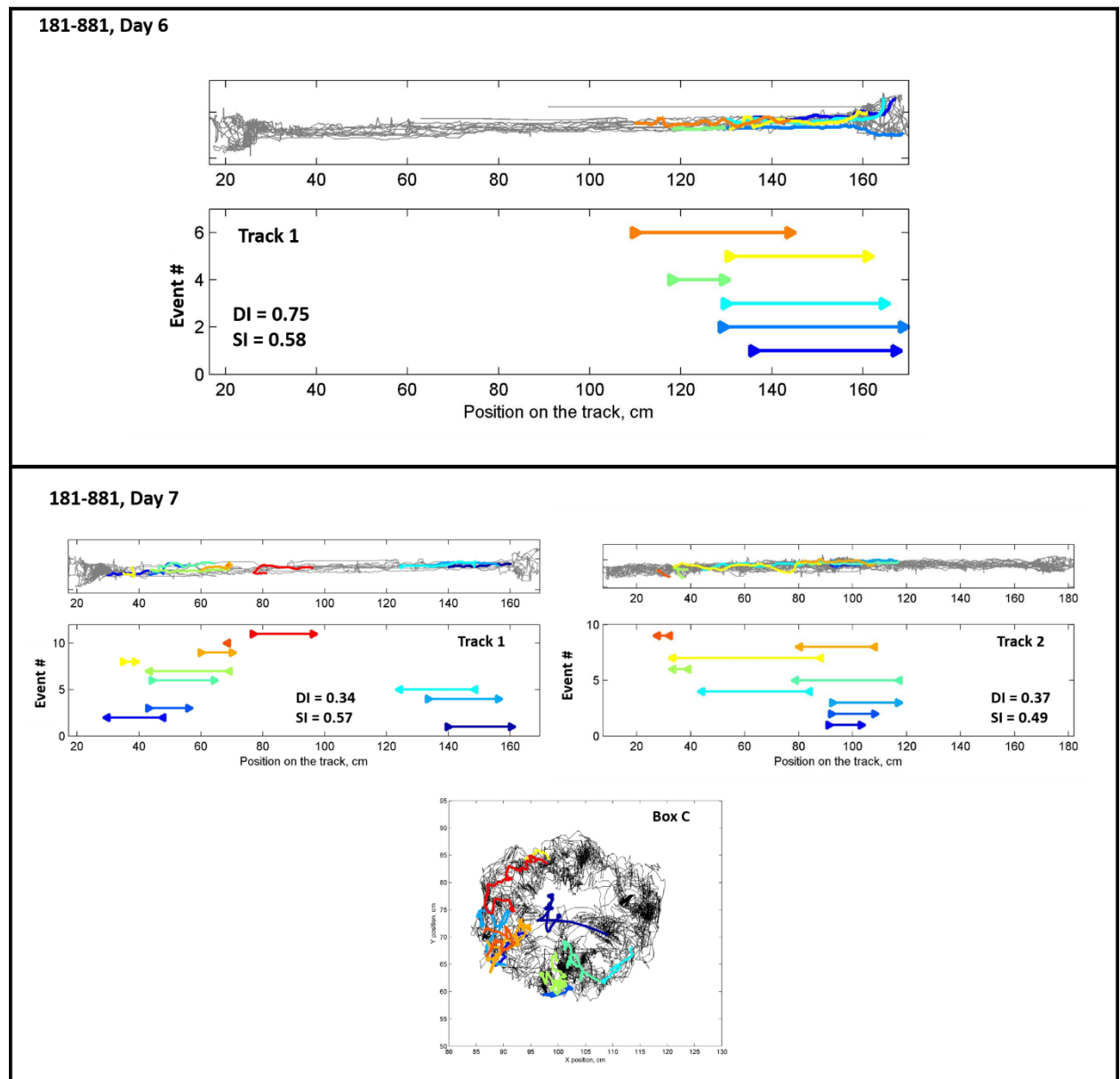


Figure S4 (cont.)

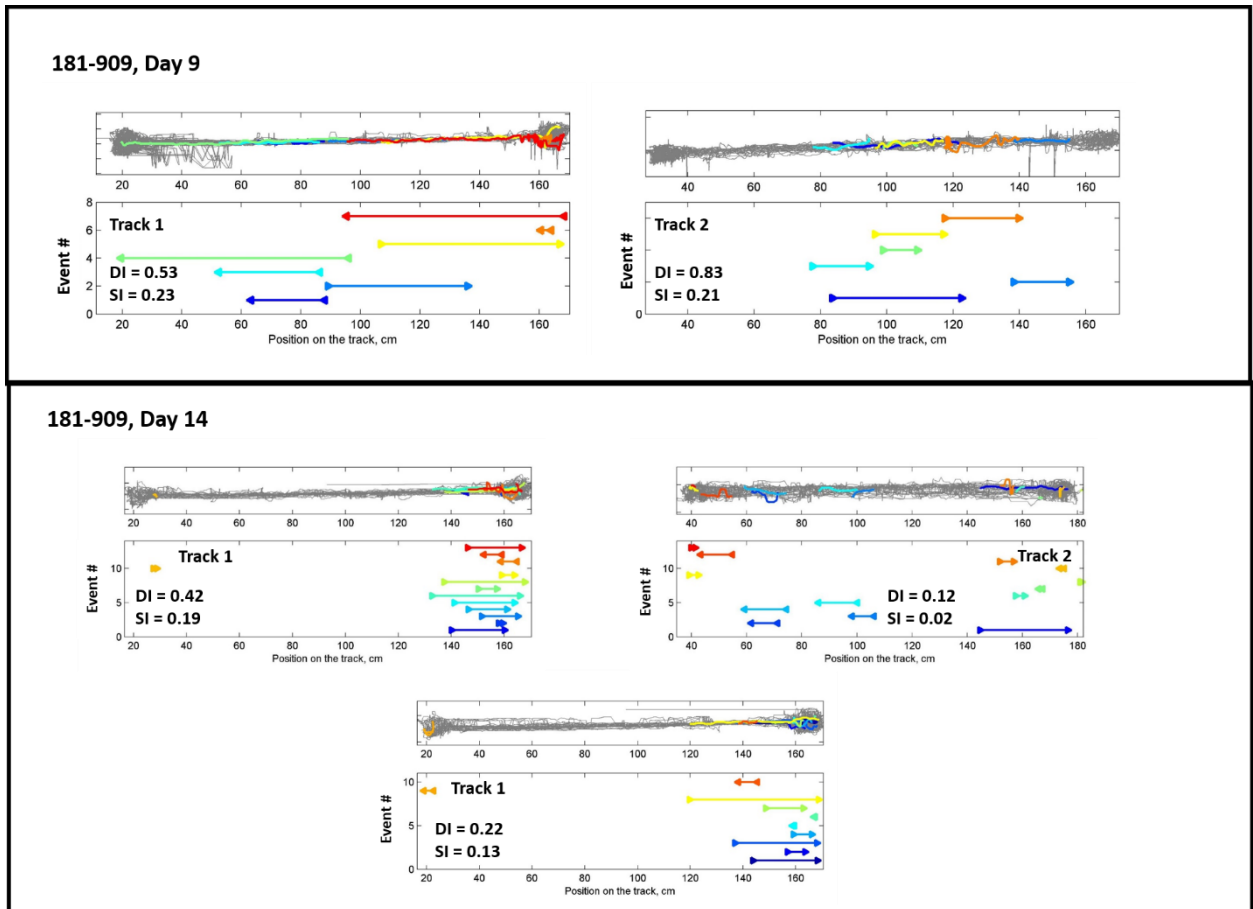


Figure S4 (cont.)

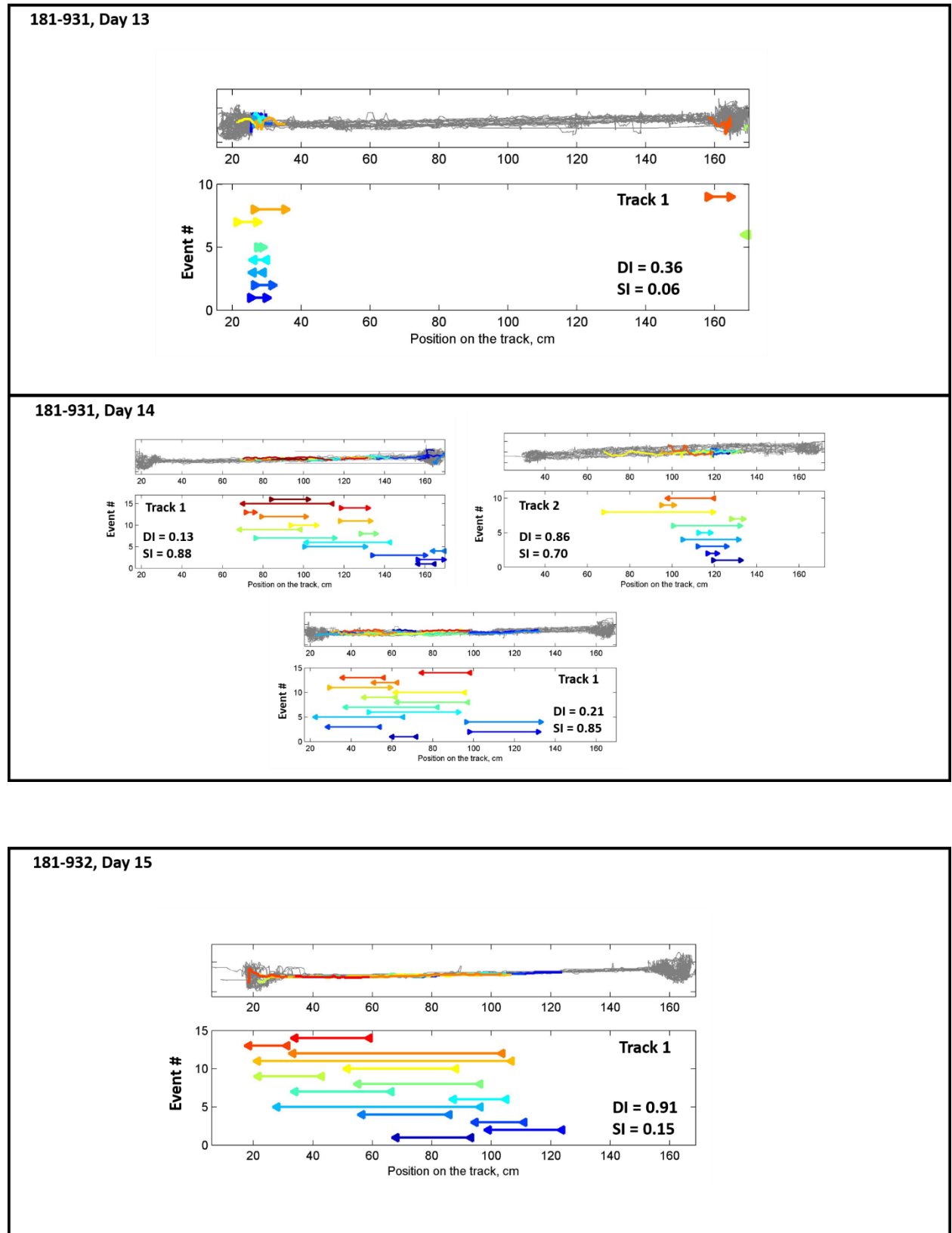
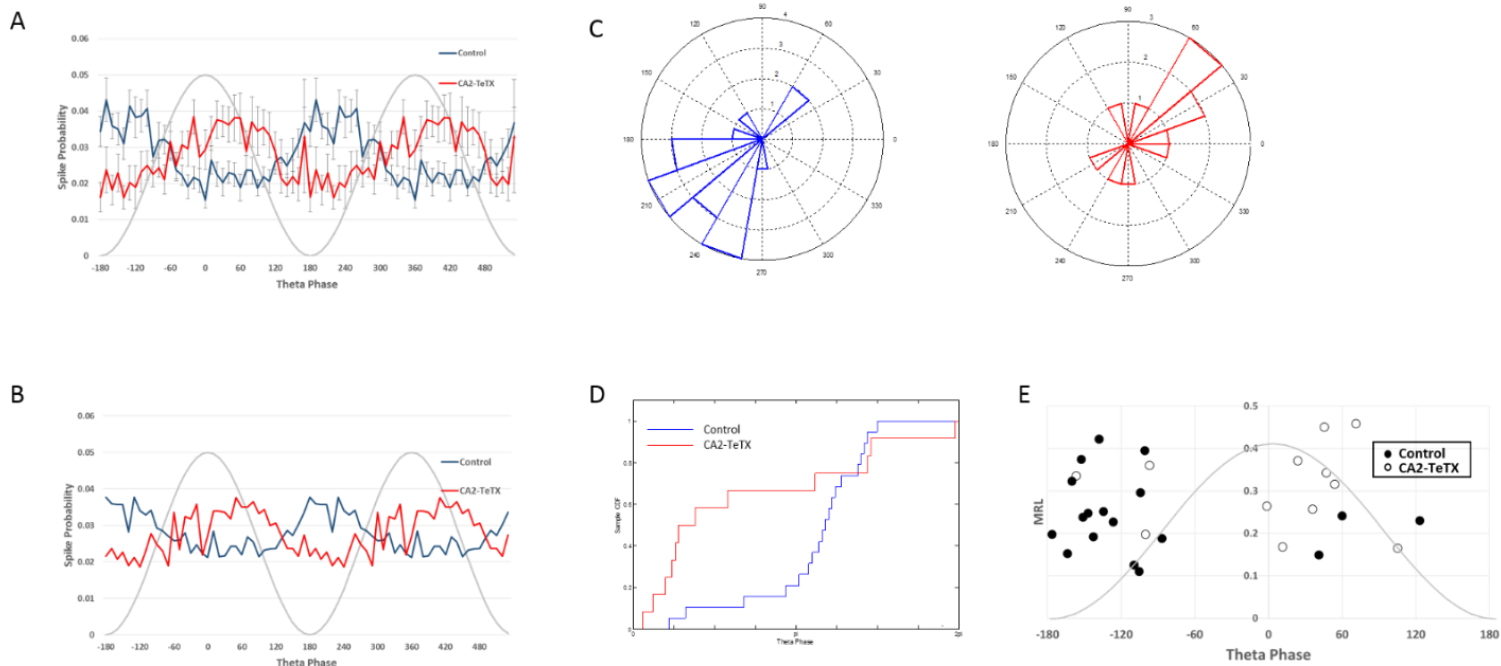


Fig. S5 Changes in Spike Timing in CA3c of CA2-TeTX Mice, Related to Figure 4



(A) In CA2-TeTX mice the spike probability of significantly theta-modulated neurons in CA3c occurs close to the peak of CA1 theta. Plot shows mean \pm SEM

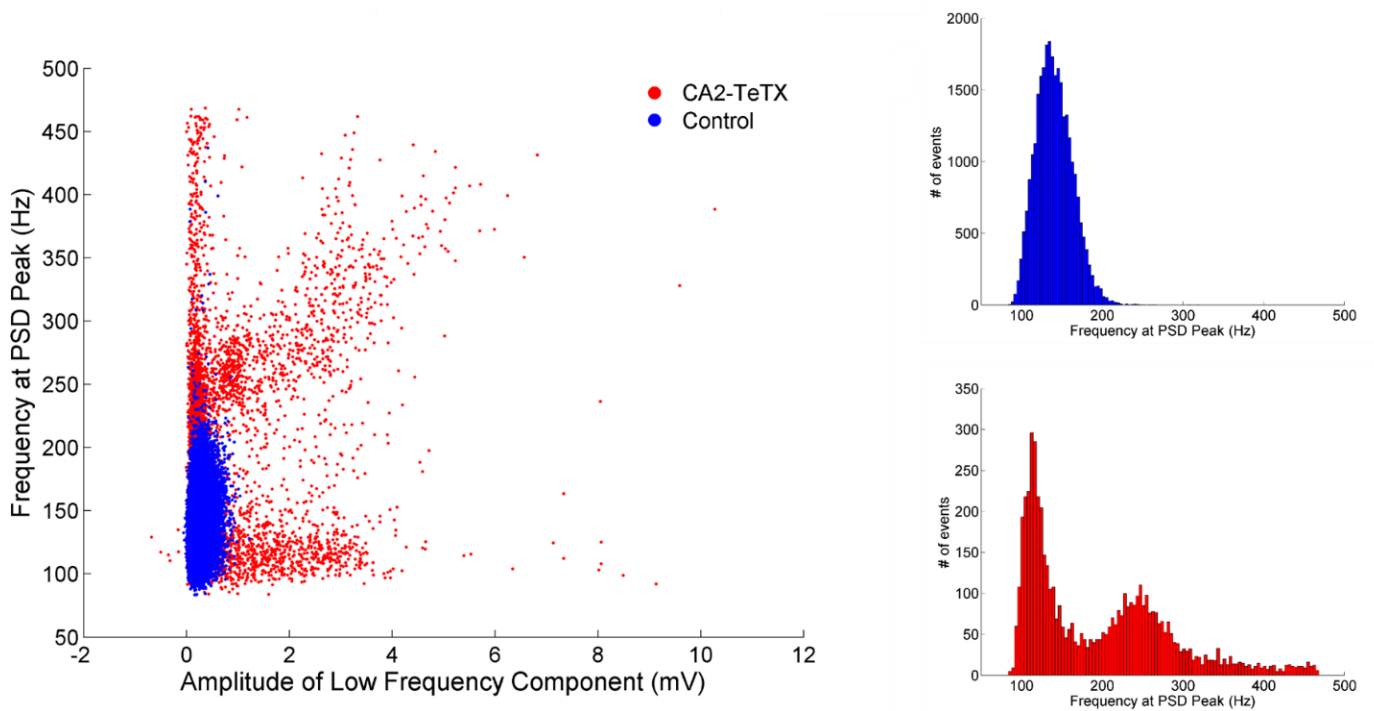
(B) A similar shift in spike probability can be seen when using spikes from all recorded CA3c pyramidal cells, regardless of the significance of theta modulation.

(C) Circular histograms of preferred phase of significantly modulated CA3c PCs in Control (blue) and CA3-TeTX (red) mice.

(D) Cumulative distribution function of preferred theta phase of CA3c neurons in Control (blue) and CA3-TeTX (red) mice.

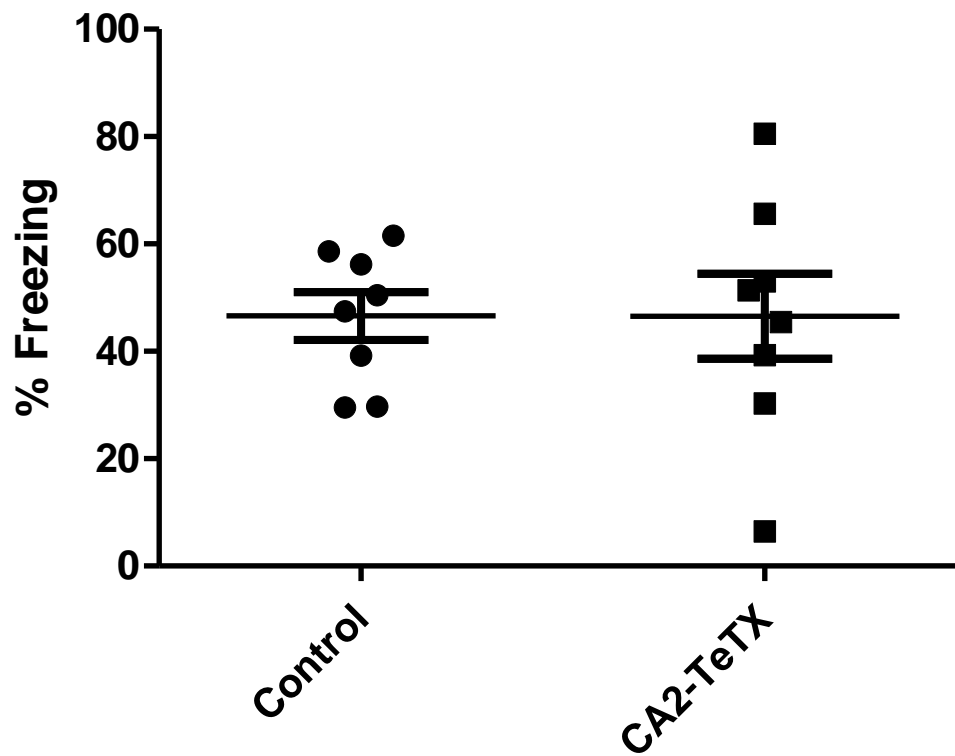
(E) Strength of theta modulation (MRL) plotted by preferred phase for significantly theta modulated CA3c pyramidal cells in Control (black) and CA2-TeTX (white) mice.

Figure S6 Chronic CA2 Silencing Leads to the Appearance of CA1 Interictal Epileptiform Discharges, Related to Figure 6



High-frequency events detected during rest sessions were identified and band-pass filtered in a high-frequency (80-500 Hz) and low-frequency band (1-20 Hz). All events recorded in CA2-TeTX mice (red; N=8, n=5564) and Control mice (blue; N=9, n=28744) were plotted by the amplitude of the slow component as a function of the frequency of the fast component. Inset on the right: Histogram of the event number plotted against the frequency of the fast component for control (blue) and CA2-TeTX (red) mice reveals the appearance of a second event type in the TeTX expressing mice.

Figure S7. CA2 Silencing does not alter Context Fear Memory. Related to Figure 7.



Context induced freezing measured 24 hours after training was similar in Control (white) and CA2-TeTX (black) mice. Each marker represents an individual mouse, lines show mean \pm SEM, t-test, $p=0.993$.

Rest

		Mean Firing Rate (Hz)	Peak Firing Rate (Hz)	Complex Spike Index
CA1	Control (N=9, n=932)	0.58±0.03	6.98±0.34	19.9±0.4
	CA2-TeTX (N=8, n=378)	0.71±0.04****	7.51±0.55****	16.2±0.6****
CA2	Control (N=7, n=259)	0.48±0.04	9.08±0.98	23.0±0.7
	CA2-TeTX (N=7, n=150)	0.52±0.05*	8.46±1.21	15.4±0.8****
CA3	Control (N=4, n=280)	0.31±0.05	3.90±0.54	18.8±0.6
	CA2-TeTX (N=5, n=204)	0.55±0.05****	7.04±0.85****	16.9±0.8***

Track

		Mean Rate (Hz)	Peak Rate (Hz)	Complex Spike Index	Spatial Information (bits/spike)	Place Field Size (% bins above threshold)
CA1	Control (N=9, n=344)	0.99±0.05	6.25±0.19	16.8±0.6	1.53±0.04	20.6±0.8
	CA2-TeTX (N=8, n=106)	1.00±0.08	5.44±0.27	16.0±1.0	1.25±0.07***	23.8±1.7
CA2	Control (N=6, n=90)	0.87±0.09	6.99±0.57	19.9±1.0	1.81±0.08	14.3±1.0
	CA2-TeTX (N=7, n=72)	0.98±0.12	4.72±0.38*	16.6±1.2**	1.29±0.08****	23.1±2.2***
CA3	Control (N=4, n=95)	0.93±0.09	8.10±0.56	17.6±0.9	2.09±0.10	15.0±1.3
	CA2-TeTX (N=6, n=47)	0.99±0.09	4.37±0.40****	18.9±2.0	0.89±0.10***	34.3±3.0***

Table S1. Firing and spatial coding properties of CA pyramidal cells recorded in control and CA2-TeTX mice during rest (top) and exploration of familiar track (bottom). Related to Figures 3, 4 and 6. All values mean ± SEM, Mann Whitney test by virus, **p<0.01, *p<0.001, ****p<0.0001**

Rest

		Mean Firing Rate (Hz)	Peak Firing Rate (Hz)	Complex Spike Index
CA1	Control (N=6, n=203)	0.56±0.06	6.56±0.77	17.1±0.7
	CA2-DREADD (N=7, n=372)	0.50±0.04	6.74±0.66	21.1±0.7**
CA3	Control (N=4, n=54)	0.35±0.08	5.46±1.57	17.4±1.4
	CA2-DREADD(N=5, n=220)	0.27±0.04	4.54±0.62	16.9±0.7

Track

		Mean Rate (Hz)	Peak Rate (Hz)	Complex Spike Index	Spatial Information (bits/spike)	Place Field Size (% bins above threshold)
CA1	Control (N=6, n=153)	1.04±0.08	7.13±0.34	15.2±0.8	1.71±0.07	17.3±0.8
	CA2-DREADD (N=7, n=217)	1.00±0.07	8.05±0.69	17.4±0.8	1.58±0.05	16.4±0.8
CA3	Control (N=4, n=45)	0.76±0.11	7.00±0.79	16.7±1.0	2.11±0.12	11.9±1.0
	CA2-DREADD(N=5, n=108)	0.72±0.06	8.10±0.71	15.8±0.8	2.15±0.07	13.4±0.9

Table S2. Firing and spatial coding properties of CA1 and CA3 pyramidal cells recorded during rest (top) or exploration of a familiar linear track (bottom) in Control and CA2-DREADD mice following systemic CNO injection. Related to Figure 5. All values mean ± SEM, Mann Whitney test by virus, **p<0.01.

movieS1.mp4

Supplementary Movie S1. Spatially-triggered hyperexcitability in a CA2-TetX mouse (Mouse 181-932). Left of frame: The movement of the mouse on the linear track. The frame is intentionally out of focus to allow for accurate tracking of the red and green diodes affixed above the animal's head. Right frame: Raw LFP signal from 7 tetrodes positioned in the hippocampus. Signals from channel 1 (top, blue) and 4 (center, bright green) are obtained from CA1, all other tetrodes are positioned in CA2/CA3. Note the raw LFP traces are all displayed in an inverted orientation.